

Working Title: Helping on the hunt for the Neutrino Mass

Master's thesis of

Fabian Leven

at the Department of Physics
Institute of Experimental Nuclear Physics (IEKP)

Reviewer: Prof. Dr. G. Drexlin
Second Reviewer: Dr. K. Valerius
Advisor: M. Sc. M. Machatchek

July 15th 2018 – July 14th 2019

Erklärung zur Selbstständigkeit

Ich versichere, dass ich diese Arbeit selbstständig verfasst habe und keine anderen als die angegebenen Quellen und Hilfsmittel benutzt habe, die wörtlich oder inhaltlich übernommenen Stellen als solche kenntlich gemacht und die Satzung des KIT zur Sicherung guter wissenschaftlicher Praxis in der gültigen Fassung vom 27.11.2014 beachtet habe.

Karlsruhe, den 14.07.2019, _____
Fabian Leven

Als Prüfungsexemplar genehmigt von

Karlsruhe, den 14.07.2019, _____
Prof. Dr. G. Drexlin

Contents

1. Neutrino Physics	1
1.1. Neutrinos until the 1960s	1
1.2. Neutrinos in the Standard Model of Particle Physics	2
1.2.1. Flavors	3
1.2.2. Mass Generating Mechanisms	4
1.3. Neutrino Oscillations	4
1.3.1. Demonstrative Formalism	4
1.3.2. Solar Neutrino Experiments	5
1.3.3. Mixing Parameters and Mass Ordering	6
1.4. Absolute Neutrino Mass Measurements	7
2. The KATRIN Experiment	9
2.1. Introduction	9
2.2. Experimental Setup	9
2.2.1. Windowless Gaseous Tritium Source	10
2.2.2. Rear Section	11
2.2.3. Differential Pumping Section	12
2.2.4. Cryogenic Pumping Section	13
2.2.5. Pre and Main Spectrometer	14
2.2.6. Detector Section	16
2.3. Modelling of the Integrated β Decay Spectrum with SSC	17
2.3.1. β Decay Spectrum	17
2.3.2. Detector Counts	18
2.3.3. Discretization of the WGTS Volume	19
2.3.4. Magnetic Bottle Effect	19
2.3.5. Scattering Probabilities	20
2.3.6. MAC-E Principle and Transmission Function	21
2.3.7. Response Function	22
2.3.8. Energy Loss Function	23
2.3.9. Distribution of Pitch Angles	23
2.3.10. Reconciliation	25
2.3.11. Amendments	25
2.4. A KATRIN Neutrino Mass Measurement	25
3. Parameter Inference at KATRIN with KaFit	27
3.1. Introduction	27
3.2. The KATRIN Likelihood	27
3.3. Intervals	28
3.3.1. Bayesian Credible Intervals	28
3.3.2. Frequentist Confidence Intervals	28
3.4. Likelihood Extensions	28
3.4.1. Implementation	29

3.4.2. Combination of Measurements	29
3.5. Overview of Analysis Methods	30
3.6. Inference Algorithms	30
3.6.1. Classical Minimizer	30
3.6.2. Markov-Chain-Monte-Carlo	30
3.7. Treatment of Uncertainties	30
3.7.1. Nuisance Parameters	30
3.7.2. Penalized Likelihood and Priors	30
3.7.3. Monte Carlo Propagation and Covariance Matrix Approach	31
3.7.4. Shift Method	31
4. Energy-Dependence of the Inelastic Scattering Cross Section	33
4.1. Introduction	33
4.2. Cross Section Values	33
4.3. Motivation	34
4.4. Scattering Probabilities	35
4.4.1. Modelling	35
4.5. Performance and Accuracy Considerations	37
4.6. Effect on Neutrino Mass Determination	38
4.7. Conclusion and Outlook	38
5. (Theoretical Corrections to the β Decay Spectrum)	43
5.1. Motivation	43
5.2. Application to Data	43
6. (Energy Loss Normalization on First Tritium)	45
7. Studies using the Preliminary KATRIN Energy Loss Model	47
7.1. The Preliminary KATRIN Energy Loss Model	47
7.2. Neutrino Mass Sensitivity	47
7.2.1. Motivation	47
7.2.2. Methodology	47
7.2.3. Model Configuration	47
7.2.4. Results	47
7.3. Application to Data	47
8. Conclusions	49
Appendix	51
A. Energy-Dependence of the Scattering Probabilities	51
A.1. Numerical Evaluation	52
B. First Tritium Data	52

List of Figures

1.1.	Standard Model of particle physics	3
1.2.	Mixing parameters and mass ordering	6
2.1.	KATRIN beamline	10
2.2.	KATRIN windowless gaseous tritium source (WGTS)	11
2.3.	KATRIN rear section	12
2.4.	KATRIN differential pumping section (DPS)	13
2.5.	KATRIN cryogenic pumping section (CPS)	14
2.6.	KATRIN detector section	16
2.7.	Tritium β spectrum	17
2.8.	Schematic of the KATRIN main spectrometer and the MAC-E principle.	21
2.9.	KATRIN response function	24
4.1.	Inelastic cross section for non-relativistic electrons scattering from molecular hydrogen isotopologues	34
4.2.	Scattering probabilities	39
4.3.	Run times comparison between using an energy dependent and independent cross section	40
4.4.	Neutrino mass shift due to an energy dependent inelastic scattering cross section	41
A.1.	Numerical accuracy of the extended model for the scattering probabilities .	53

List of Tables

1.1.	Gauge field content of the Standard Model	2
1.2.	Matter field content of the Standard Model	2
4.1.	Energy-dependence of the inelastic scattering cross section	35
4.2.	Scattering probabilities	35

1. Neutrino Physics

1.1. Neutrinos until the 1960s

The rich history of neutrino physics covers more than a century. The following paragraphs outline selected milestones on the way to their today's understanding.

In 1895 Becquerel reported results on experiments with phosphorescent substances, especially uranium salts, on photographic plates [Bec95]. His experiments are marked as the discovery of radioactivity and triggered manifold subsequent investigations.

In 1899 Rutherford published a classification of radioactive decays into α and β types according to their penetration strength [Rut99].

In 1900 Becquerel determined the mass-charge-ratio of β decay particles and identified them as the electron previously described by Thomson [Bec00] [Tho97].

In 1914 Chadwick measured a continuous electron energy spectrum in the β decay (β spectrum) of lead-214 and bismuth-214 [Cha14].

In 1927 Ellis and Wooster conducted a calorimetric measurement of the β decay energy of radium and demonstrated that the continuity of the β spectrum was intrinsic to the decay as opposed to caused by secondary effects as e.g. scattering of the electrons within an atom [EW72].

In 1930 a β decay was thought of as a two-body-decay $A \rightarrow B + C$. Assuming relativistic kinematics, especially conservation of energy and momentum, in a two-body-decay the momenta of the daughter particles B and C are solely determined by their masses and the energy constitution of the parent particle A . According to Bohr there was no reason to believe that different nuclei of the same element A should have a different energy constitution in a β decay. Hence, the continuity of the β spectrum could not be explained [Boh32]. As a possible solution Pauli suggested the β decay to be a three-body-decay and postulated a electrically neutral particle that carries part of the decay energy [PW+08].

In 1934 Fermi developed a quantitative theory of β decay that could describe the preceding experimental results. It comprises a four-fermion contact interaction respectively a three-body-decay model. It was the first description of the so-called “weak interaction”. Furthermore, Fermi coined the term “neutrino” for the particle postulated by Pauli. [Fer34]

Fermi's theory inspired the idea to use the so-called “inverse β decay” or “neutrino capture” to detect neutrinos, which in today's nomenclature is written as

$$\bar{\nu}_e + p^+ \rightarrow n + e^+.$$

In 1956 Cowan and Reines published results of a corresponding experiment. It was conducted using the sufficiently high neutrino flux of the nuclear reactor of the Savannah River Plant. The neutrinos originating in the reactor passed a tank of water and cadmium

Table 1.1.: Gauge field content of the Standard Model of particle physics.

symbol	gauge symmetry	associated charge
g	SU(3)	color
W	SU(2)	isospin $\mathbf{T} = (T_1, T_2, T_3)$
B	U(1)	hypercharge Y

Table 1.2.: Matter field content of the Standard Model of particle physics and corresponding properties (color charge omitted).

symbol	spin	generations	isospin ($ \mathbf{T} , T_3$)	hypercharge Y
higgs	$\phi = (\phi^+, \phi^0)^T$	0	1 ($1/2, \pm 1/2$)	$\pm 1/2$
quark	$q = (u_L, d_L)^T$	1/2	3 ($1/2, \pm 1/2$)	$\pm 1/3$
antiquark	\bar{d}_R	1/2	3 (0, 0)	+1/6
	\bar{u}_R	1/2	3 (0, 0)	-4/3
lepton	$l = (\nu_L, l_L)^T$	1/2	3 ($1/2, \pm 1/2$)	$\mp 1/2$
antilepton	\bar{l}_R	1/2	3 (0, 0)	+2

chloride triggering the above process. The emerging neutron was captured by the cadmium which emitted a photon in a 3 MeV to 11 MeV range. The emerging positron annihilated with an electron which produced two photons of 0.5 MeV each. A coincidence measurement of the corresponding photons enabled discriminating signal and background events. Based on their results they reported the free neutrino's discovery. [CR+56]

In the same year, 1956, Lee and Yang published an article on parity conservation. Parity conservation implies that a mirrored physical process behaves the same as its non-mirrored counterpart. They pointed out that parity conservation might be violated in weak interactions and suggested several probing methods. [LY56]

In 1957 Wu et. al. conducted one of the corresponding probing methods based on β decay. The parity operation respectively "the mirroring" corresponded a change of the magnetic field orientation in the experiment. The results showed that parity is violated. [WA+57]

In 1958 Goldhaber et al. measured the helicity H of the neutrino. Its helicity is defined as $H = \hat{\sigma} \cdot \hat{\mathbf{p}}$, where $\hat{\sigma}$ is the spin unit vector and $\hat{\mathbf{p}}$ is the momentum unit vector of the neutrino. The experiment found $H = -1$ which corresponds a maximal parity violation. In other words, only left-handed neutrinos and right-handed antineutrinos interact weakly. [GG+58]

In 1962 Danby et. al. reported on a second type of neutrinos. A beam of pions generated at the Alternating Gradient Synchrotron in Brookhaven decayed according to $\pi^\pm \rightarrow \mu^\pm + \nu/\bar{\nu}$. The emerging neutrinos penetrated a 13.5-meter iron shield wall and their interaction could be detected in a 10-t aluminum spark chamber. The observed interactions were path-like as opposed to shower-like, which implied the production of muons as opposed to electrons. This was marked as the discovery of the μ neutrino. [DG+62]

The attempts to uniformly describe the manifold discoveries in the field of particle physics in a combined theory converged over the course of the second half of the 20th century into the so-called Standard Model of particle physics (SM).

1.2. Neutrinos in the Standard Model of Particle Physics

The Standard Model of particle physics is a well-tested and established theory, which is evident by e.g. the extensive Review of Particle Physics of the Particle Data Group [Tan+18].

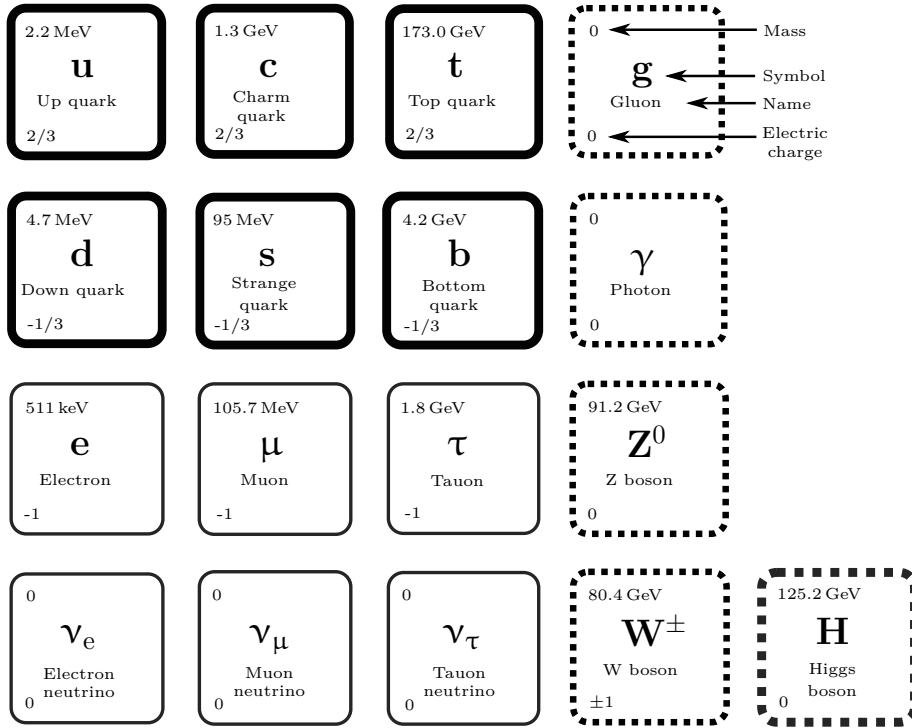


Figure 1.1.: Standard Model of particle physics. The fermions are framed continuous and the bosons dotted. Among the fermions the quark sector is marked by a thick frame and the lepton sector by a thin one. (Illustration adapted from [Sei19])

It is a gauge quantum field theory exhibiting the gauge symmetry $SU(3) \times SU(2) \times U(1)$. Table 1.1 contains the SM's gauge fields and their associated charges. The B - and W -fields mix to the observable W^+ , W^- and Z^0 bosons as well as to the photon γ . Table 1.2 contains the SM's matter fields and their properties.

Experimentally, a “disturbance” of a quantum field is often localized in space-time, which makes it practical to speak of the SM’s content as particles with intrinsic properties. Figure 1.1 depicts the particles of the SM along with their masses and electric charge.

In the SM neutrinos are leptons with the following properties:

flavors	3 (ν_e, ν_μ, ν_τ)
electric charge	0 (neutral)
spin	$\frac{1}{2}\hbar$ (fermion)
helicity	left-handed neutrinos right-handed antineutrinos

1.2.1. Flavors

A particle’s flavor is its eigenstate with respect to the weak interaction. In the 1990s a precision measurement of the width of the Z^0 -boson resonance at the Large Electron Positron Collider (LEP) yielded a number of light neutrino flavours consistent with 3 [Acc+98]. In this context “light” refers to a neutrino mass smaller than half the mass of the Z^0 boson. The SM incorporates these three flavors, usually labeled ν_e , ν_μ and ν_τ . The last one to be discovered was the τ neutrino in 2001 by the DONUT collaboration [Kod+01].

1.2.2. Mass Generating Mechanisms

For a theory to account for neutrino masses its Lagrangian density must exhibit corresponding mass terms. According to [Zub11] the formalism can be summarized: The form of a mass term is given by the Dirac equation, which is produced by applying the principle of least action to a suitable Lagrangian density \mathcal{L} . The mass terms have to be quadratic in the fermion fields ψ and must leave the Lagrangian density hermitian. Furthermore, a field ψ must have a left- and right-handed component in order for the mass terms not to vanish. Two possible term forms are named after Dirac and Majorana. Whether one or a mixture of both forms correspond the neutrino's reality is an open question.

Dirac Masses

A Dirac mass term with mass m_D split in its chiral components (Weyl spinors) $\psi_{L,R}$ has the form

$$\mathcal{L}_D = -m_D \bar{\psi} \psi = -m_D (\bar{\psi}_L \psi_R + \bar{\psi}_R \psi_L). \quad (1.1)$$

Applying this to neutrinos it requires both, a left- and a right-handed Dirac neutrino. Right-handed neutrinos have not yet been observed. If they exist, they don't interact weakly and hence, are called sterile.

Majorana Masses

For Majorana mass terms, one uses the CP-conjugate ψ^C of a fermion spinor ψ . Note that if ψ is left-handed, ψ^C is right-handed and vice versa. One can then define a Majorana field ϕ and construct a corresponding mass term \mathcal{L}_M with a mass m_M

$$\phi = \psi + \psi^C \quad \mathcal{L}_M = -\frac{1}{2} m_M \bar{\phi} \phi. \quad (1.2)$$

As $\phi^C = \phi$, the described Majorana particle is its own antiparticle, which due to charge conservation is only possible for neutral particles, such as a neutrino.

1.3. Neutrino Oscillations

1.3.1. Demonstrative Formalism

According to [Zub11] a formula demonstrating neutrino oscillations can be derived: If the neutrino's mass eigenstates $|\nu_i\rangle$ ($i \in \{1, 2, 3\}$) of the free Hamiltonian differ from their flavor eigenstates $|\nu_\alpha\rangle$ ($\alpha \in \{e, \mu, \tau\}$) of the weak interaction, neutrinos oscillate in flavor space. The corresponding matrix for a basis change U is called Pontecorvo-Maki-Nakagawa-Sakata matrix (PMNS matrix)

$$|\nu_\alpha\rangle = \sum_i U_{\alpha i} |\nu_i\rangle. \quad (1.3)$$

The PMNS matrix U is commonly parametrized using three angles $\theta_{12}, \theta_{23}, \theta_{13} \in [0, 2\pi]$, a CP-violating phase $\delta \in [0, 2\pi]$ and two Majorana phases $\alpha, \beta \in [0, 2\pi]$:

$$U = \begin{pmatrix} 1 & 0 & 0 \\ 0 & \cos \theta_{23} & \sin \theta_{23} \\ 0 & -\sin \theta_{23} & \cos \theta_{23} \end{pmatrix} \begin{pmatrix} \cos \theta_{13} & 0 & \sin \theta_{13} e^{-i\delta} \\ 0 & 1 & 0 \\ -\sin \theta_{13} e^{i\delta} & 0 & \cos \theta_{13} \end{pmatrix} \begin{pmatrix} \cos \theta_{12} & \sin \theta_{12} & 0 \\ -\sin \theta_{12} & \cos \theta_{12} & 0 \\ 0 & 0 & 1 \end{pmatrix} \begin{pmatrix} 1 & 0 & 0 \\ 0 & e^{i\alpha} & 0 \\ 0 & 0 & e^{i\beta} \end{pmatrix}. \quad (1.4)$$

The evolution of a neutrino's flavor state on a 1-dimensional path starting at position $x = 0$ at time $t = 0$ with momentum p_i and energy E_i of its mass eigenstates $|\nu_i\rangle$ is

$$|\nu_\alpha(x, t)\rangle = \sum_i U_{\alpha i} e^{-i(E_i t - p_i x)} |\nu_i\rangle. \quad (1.5)$$

This leads to the transition amplitudes

$$A(\alpha \rightarrow \beta)(t) = \langle \nu_\beta | \nu_\alpha(L) \rangle = \sum_i U_{\beta i}^* U_{\alpha i} e^{-i(E_i t - p_i x)t} \quad (1.6a)$$

$$A(\bar{\alpha} \rightarrow \bar{\beta})(t) = \langle \bar{\nu}_\beta | \bar{\nu}_\alpha(L) \rangle = \sum_i U_{\beta i} U_{\alpha i}^* e^{-i(E_i t - p_i x)t}. \quad (1.6b)$$

If $\delta \neq 0$ ($\Rightarrow U \neq U^*$), (1.6) implies CP -violation.

The following assumptions allow for a demonstrative form of the transition probability:

- The neutrinos are relativistic:
 - Their momentum equals approximately their energy which is by far larger than their mass $p_i \approx E_i \gg m_i$. This also implies the energy can be expanded in the mass-momentum-ratio m_i/p_i .
 - They travel the distance $x = L = ct$ at the speed of light c .
- All neutrino generations have approximately the same momentum $E \approx p \approx p_i$.
- The CP -violating phase vanishes $\delta = 0$.

Then, the transition probability from one flavor α to another β is

$$\begin{aligned} P(\alpha \rightarrow \beta)(L) &= |\langle \nu_\beta | \nu_\alpha(L) \rangle|^2 \\ &= \delta_{\alpha\beta} - 4 \sum_i \sum_{j>i} U_{\alpha i} U_{\alpha j} U_{\beta i} U_{\beta j} \sin^2 \left(\frac{(m_i^2 - m_j^2)}{4} \frac{L}{E} \right). \end{aligned} \quad (1.7)$$

Equation (1.7) shows oscillatory behavior if the mass of at least two flavors differ and the corresponding off-diagonal elements of the PMNS matrix U are non-vanishing. Furthermore, neutrino oscillation experiments are sensitive to the difference of squared masses

$$\Delta m_{ij}^2 = |m_i^2 - m_j^2|. \quad (1.8)$$

which only yields two independent observables for three masses. Thus, these experiments can not be used to determine the absolute mass scale of neutrinos.

1.3.2. Solar Neutrino Experiments

Solar neutrino experiments led to the discovery of neutrino oscillations. In the end of the 1930s Bethe, von Weizsäcker and Critchfield showed that the so-called pp cycle is the primary source of solar neutrinos [Wei38; BC38; Bet39]. Its initial reaction and the one with the broadest neutrino energy spectrum are



Note that only electron neutrinos are produced in the sun. Starting from the 1970s the solar neutrino flux was measured; the first time by the Homestake experiment using the inverse beta decay of ${}^{37}\text{Cl}$. It could detect electron neutrinos with an energy threshold of 813 keV. The flux was one third of the prediction by the standard solar model [CD+98]. The experiments GALLEX/GNO and SAGE confirmed the results, where the later could

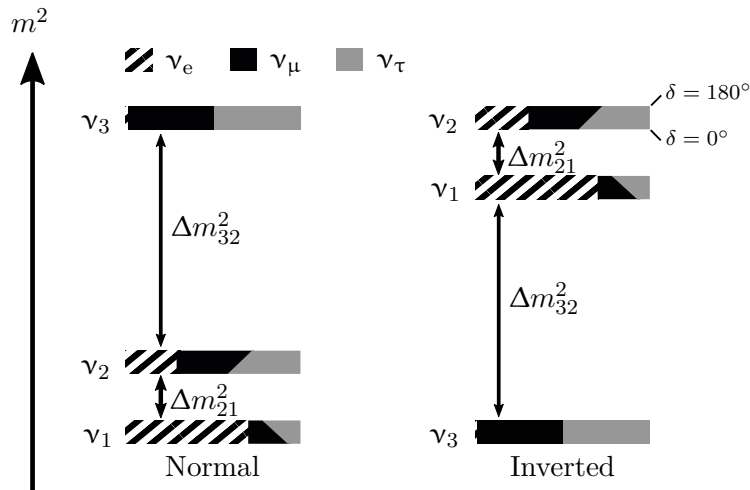


Figure 1.2.: Mixing parameters and mass ordering. The chart shows how the mass eigenstates ν_i are composed of the flavor eigenstates ν_α in the normal and inverted mass ordering. The composition depends on the phase δ . The mixing is shown for the two extreme cases $\delta = 0^\circ$ (baseline) and $\delta = 180^\circ$ (topline). Note that the mass splitting is not to scale. (Adapted from [Sei19]. Numerical values can be found in [EG+19].)

detect electron neutrinos with an energy threshold of 233 keV [Kir98; AB+05; AG+09]. Starting from 1999 the SNO experiment measured the neutrino flux of all flavors. It used 1000 t of heavy water D₂O to detect electron neutrinos via charged currents as well as all flavors via neutral currents and neutrino-electron scattering. The measured flux of all flavors of the ⁸B neutrinos (1.9) was in accordance with the electron neutrino flux predicted by the standard solar model [AA+13]. Accounting for neutrino oscillations in free space as well as matter mediated (MSW effect [Wol78; MS86]) explains the flux data. All in all, neutrino oscillations are experimentally verified and proof that neutrinos have mass.

1.3.3. Mixing Parameters and Mass Ordering

According to (1.7) the ratio L/E determines the sensitivity of an experiment to the PMNS matrix U (mixing parameters) and to Δm_{ij}^2 (mass ordering). L can be tuned by placing the detector in a suitable distance from the neutrino source. E can either be tuned by using e.g. particle accelerators as source or if the source exhibits an energy spectrum like e.g. the sun. According to [Zub11] there are four major neutrino sources that can be used to measure the mixing parameters and the mass ordering:

source	flavors	sensitive to
nuclear power plants	$\bar{\nu}_e$	$\sin \theta_{13}$
accelerators	$\nu_e, \nu_\mu, \bar{\nu}_e, \bar{\nu}_\mu$	$\sin \theta_{23}, \Delta m_{23}^2$
atmosphere	$\nu_e, \nu_\mu, \bar{\nu}_e, \bar{\nu}_\mu$	$\sin \theta_{23}, \Delta m_{23}^2$
Sun	ν_e	$\sin \theta_{12}, \Delta m_{21}^2$

Furthermore, the MSW resonance of solar neutrinos requires $m_1 < m_2$, which allows for two possible mass orderings:

1. normal ordering $m_1 < m_2 < m_3$ and
2. inverted ordering $m_3 < m_1 < m_2$.

A combination of recent experimental results can be found in [EG+19]. Figure 1.2 illustrates the mixing parameters and the mass ordering. For normal ordering the best fit for the

phase is $\delta = 215^\circ$, but CP-conservation ($\delta = 180^\circ$) can not be ruled out. Furthermore, $\Delta m_{21}^2 \approx 7 \times 10^{-5} \text{ eV}^2$ and $\Delta m_{23}^2 \approx 2 \times 10^{-3} \text{ eV}^2$.

1.4. Absolute Neutrino Mass Measurements

Measurements of the absolute neutrino mass fall into one of three categories [OW08]:

- cosmology,
- neutrinoless double β decay or
- kinematic measurements.

Cosmology

In the early Universe neutral particles such as light neutrinos could escape from areas of high density to areas of low density. As they carry away mass, the larger the neutrino mass m_ν , the stronger is the suppression of density fluctuations on small scales. In a mathematical formulation the so called power spectrum of the density contrast is examined. Corresponding data are e.g. obtained by the Sloan Digital Sky Survey (SDSS). This experiment records the sky's electromagnetic spectrum via telescope [DT+04]. Furthermore, the temperature anisotropies in the cosmic microwave background (CMB) encode information on the Universe's structure. The latest and most precise data are recorded by the PLANCK satellite [Agh+18]. Under the assumption that all mass states contribute with the same number density cosmological observations are to first order only sensitive to the sum of all neutrino masses $\sum_i m_i$. A combination of the above data sets yields [YP+17]

$$\sum_i m_i < 0.14 \text{ eV} \quad (95\% \text{ C.L.}) .$$

Neutrinoless Double β Decay

Double β decay ($2\nu\beta\beta$) is described as a nucleus of element $X(Z, A)$ with Z protons and $A - Z$ neutrons that decays to a daughter isotope $Y(Z + 2, A)$ via two simultaneous β decays

$$X(Z, A) \rightarrow Y(Z + 2, A) + 2e^- + 2\bar{\nu}_e . \quad (1.10)$$

According to [Zub11] if the neutrino is its own antiparticle, the neutrino emitted in the first decay can be absorbed in the second decay resulting in a neutrinoless double decay ($0\nu\beta\beta$). This would require the neutrino to have mass and be of Majorana type. Such a decay would manifest itself in a peak in the β spectrum two neutrino masses above the endpoint of the continuum. Note that this would violate lepton number conservation. The half-life of such a decay encodes the Majorana mass of the electron neutrino as a weighted sum of all neutrino masses using the PMNS matrix U (1.4)

$$m_{\beta\beta} = \left| \sum_i U_{ei}^2 m_i \right| . \quad (1.11)$$

Note that U contains two unknown Majorana phases that might cause cancellation in (1.11). This makes it difficult to compare $m_{\beta\beta}$ to masses obtained by other methods. The two most stringent upper limits on $m_{\beta\beta}$ are given as ranges by:

experiment	90 % C.L. upper limit on $m_{\beta\beta}$ [eV]
GERDA [Ago+18]	0.12–0.26
KamLAND-Zen [GG+16]	0.05–0.16

Kinematic Measurements

In decay processes the mass of neutrinos manifests itself in their energy spectrum or the energy spectrum of other decay products. With currently achievable energy resolutions the corresponding observable is a weighted sum of the N neutrino eigenmasses where the weights are the elements of the PMNS matrix (1.4)

$$m_{\nu_\alpha}^2 = \sum_i^N |U_{\alpha i}|^2 m_i^2. \quad (1.12)$$

An experiment with a sufficiently high energy resolution can be sensitive to terms of the above sum (1.12). This enables the search for sterile neutrinos ($N > 3$). A summary of kinematic neutrino mass experiments can be found in [OW08; Sei19; Zub11], of which a selection is:

- **Neutrinos from Supernova 1987A**

One would expect higher energetic neutrinos to arrive on Earth earlier than lower energetic ones, which was observed by multiple experiments. A corresponding analysis yielded an upper limit for the mass of the electron neutrino [LL02]

$$m_{\nu_e} < 5.7 \text{ eV} \quad (95\% \text{ credible interval}).$$

- **Muon decay**

At the Paul Scherrer Institute the decay of pions to muons and muon neutrinos was examined. An analysis of the momenta yielded an upper limit on the muon neutrino mass [AB+96]

$$m_{\nu_\mu} < 17 \text{ keV} \quad (90\% \text{ C.L.}).$$

- **Tauon decay**

At the LEP the decay of tauons to pions and tau neutrinos was examined. An analysis of the momenta yielded an upper limit on the tauon neutrino mass [Bar+98]

$$m_{\nu_\tau} < 18.2 \text{ MeV} \quad (95\% \text{ C.L.}).$$

- **β decay**

In β^- decay

$$X(Z, A) \rightarrow Y(Z + 1, A) + e^- + \bar{\nu}_e \quad (1.13)$$

part of the released surplus energy generates the neutrino's mass. This leaves a signature in the β spectrum. The latest two experiments investigated tritium β decay in Mainz and Troitsk and yielded a combined result of [KB+05; Ase+11; Tan+18]

$$m_{\nu_e} < 2 \text{ eV} \quad (95\% \text{ C.L.}).$$

Note that KATRIN is a successor of these two experiments and aims for an even better precision of $m_{\nu_e} < 0.2 \text{ eV}$ (90 % C.L.) [Ang+05].

2. The KATRIN Experiment

2.1. Introduction

The KArlsruhe TRItium Neutrino (KATRIN) experiment performs a kinematic measurement of the tritium β spectrum in order to determine the mass of the electron antineutrino (from here forth labeled m_ν) as defined by equation (1.12). In case no neutrino mass signal is observed, KATRIN aims to set a an upper limit of

$$m_\nu < 200 \text{ meV} \quad (90\% \text{ C.L.})$$

which is one order of magnitude lower than the one by its predecessor experiments. (See section 1.4.) KATRIN recorded the first β spectrum in March 2018 and started neutrino mass measurements in March 2019.

2.2. Experimental Setup

The KATRIN experiment has a 70 m beam line which is depicted in figure 2.1. It can be divided into two sections:

1. Within the **source and transport section (STS)** the tritium decays and the β electrons are magnetically guided to the
2. **spectrometer and detector section (SDS)** where they are filtered out according to their kinetic energy and finally counted at the detector.

A comprehensive description of the KATRIN apparatus can be found in the KATRIN Design Report [Ang+05] supplemented by more recent hardware overviews as e.g. in [Sei19].

Some central concepts of the source section are:

Beam tube setup: In the STS the beam line is split into beam tube elements respectively stainless steel pipes. The pipes are either connected directly or by functional elements such as pump ports and valves.

Magnetic guidance of charged particles: Superconducting coils surrounding the beam line in the STS as well as coils around the spectrometer tank in the SDS create a magnetic field. The field lines are approximately parallel to the beam line and intersperse it over the range of the whole experiment. Charged particles perform cyclotron motions around the field lines and are adiabatically guided from the STS to the detector. Adiabaticity is guaranteed by avoiding strongly varying field strengths on short distances.

Temperature: Different parts and layers of the source section are operated at specific temperatures for several reasons such as establishing super-conductivity for the coils, stable gas dynamics and gas flow reduction. Several cooling systems based on liquid helium, neon, nitrogen and argon are installed. Additionally, in the STS, the beam tube, the magnets

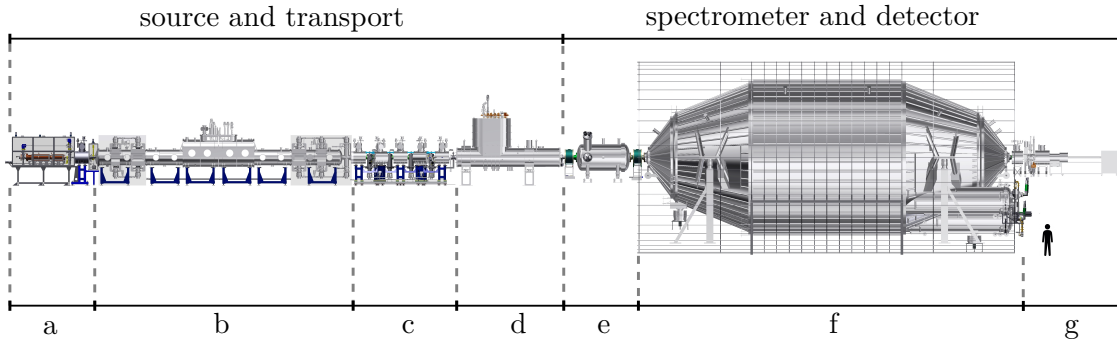


Figure 2.1.: The KATRIN beamline. Main components from south to north:

- a) rear section (see section 2.2.2)
- b) windowless gaseous tritium source (WGTS) (see section 2.2.1)
- c) differential pumping section (DPS) (see section 2.2.3)
- d) cryogenic pumping section (CPS) (see section 2.2.4)
- e) pre spectrometer (see section 2.2.5)
- f) main spectrometer (see section 2.2.5)
- g) detector (see section 2.2.6)

and the hull are separated by insulation vacuums as well as heat shields of liquid nitrogen and neon.

Gas flow: The spectrometer must be kept practically free of any tritium flow for safety and background reasons. Nonetheless, to allow an undisturbed passage of the β electrons, the spectrometer is windowlessly connected to the source section. Hence, differential pumping sections are installed that reduce the inlet pressure of $\sim 3 \times 10^{-3}$ mbar to the tritium partial pressure of $\sim 1 \times 10^{-11}$ mbar.

2.2.1. Windowless Gaseous Tritium Source

The windowless gaseous tritium source (WGTS) is a 16 m-long, 1.5 m-wide and 4 m-high cryostat. It is depicted in figure 2.2 and a detailed description can e.g. be found in [GB+08].

The inner loop: The molecular tritium (T_2) is injected centrally in the WGTS's 90 mm-wide beam tube where it decays. The design gas column density is

$$\rho d = 5 \times 10^{17} \text{ molecules/cm}^2 \quad (2.1)$$

of which

$$\epsilon_T = 95 \% \quad (2.2)$$

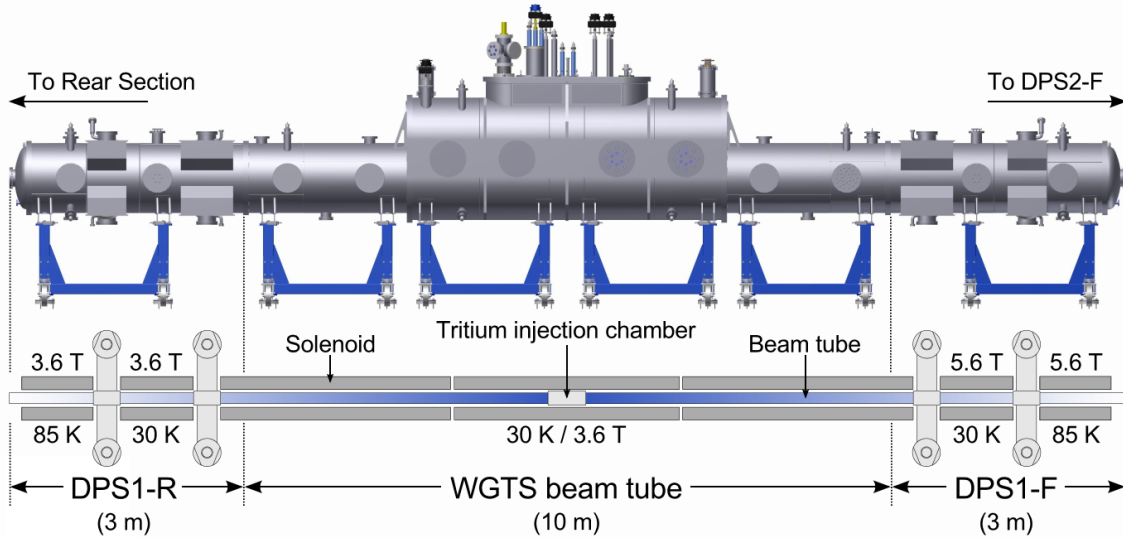


Figure 2.2.: The windowless gaseous tritium source (WGTS). Shown are the hull and a sketch of the beam tube. Indicated are the molecular pumps, the design temperatures for tritium operation, the maximum magnetic field strengths and a color gradient depicting the decreasing gas density from the center to the sides. (From [Har15])

are isotopic tritium molecules. At the front and rear of the WGTS the gas is extracted from the beam tube by molecular pumps in designated differential pumping sections called DPS-1-R (rear) and DPS-1-F (front). The extracted gas is re-injected in the center of the beam tube. The respective pipe system is called the inner loop. Selected important parts of the inner loop are:

- a buffer vessel where tritium of high purity is introduced from the feed loop of the Tritium Laboratory Karlsruhe (TLK);
- a laser Raman system (LARA) that monitors the isotopic composition of the gas;
- a pressure and temperature controlled buffer vessel to regulate the gas inlet into the WGTS; and
- a permeator that separates impurities (like e.g. helium) and ejects them into the exhaust loop of the TLK.

Magnetic field: In order to adiabatically guide the β electrons to the spectrometer section the WGTS is submerged in a magnetic field parallel to its beam tube of up to 5.6 T. It is created by 7 superconducting coils, that surround the beam tube. These magnets are kept at a temperature of 4.2 K by liquid helium.

Temperature: The stability of the column density (2.1) must be on the 0.1 % level. This requires stable parameters like temperature T and pressure p . On one hand, the higher the temperature the less stable the system. Furthermore, thermal motion smears the energy spectrum of the β electrons (Doppler effect). On the other hand, at low temperatures the gas molecules cluster. $T = 30\text{ K}$ is chosen as a compromise and established by a two-phase neon cooling system. For calibration purposes it is also possible to operate the WGTS with krypton instead of tritium. This requires a beam tube temperature of $T = 100\text{ K}$ in order for the krypton not to freeze. In this operational mode the neon has to be exchanged for argon that provides a suitable vapor pressure.

2.2.2. Rear Section

The rear section terminates the beam line in the upstream direction. It houses monitoring, calibration and control devices. It is depicted in figure 2.3 and a detailed description can

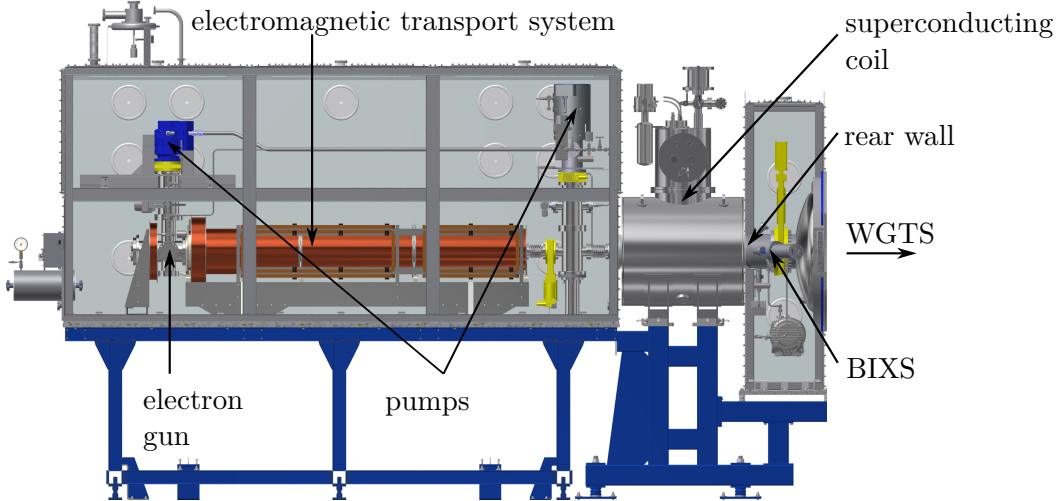


Figure 2.3.: The rear section terminates the KATRIN beam line and houses several monitoring and calibration devices. (Adapted from [Sei19])

e.g. be found in [Bab14].

Rear wall: The so-called rear wall is a gold-coated stainless-steel disc with a diameter of 6 inches that terminates the beam tube.

Electron gun: The rear section houses an electron gun in order to measure the response function of the experiment (see section 2.3.7). Its energy resolution is $\sim 0.2\text{ eV}$ and its angular resolution is $\sim 4^\circ$. The electrons' flight path can be adjusted by dipole magnets mounted in the WGTS which enables a scanning of the full beam tube.

Plasma control: Space charges, respectively a plasma, forms within the WGTS due to the tritium decay. β electrons might therefore start at different potentials which adds uncertainty to the measured β spectrum. Hence, plasma effects have to be controlled. Simulations show that the plasma can be influenced by the rear wall potential which can be controlled by a voltage supply in the range of $\pm 10\text{ V}$. Moreover, a UV light illumination of the rear wall can extract electrons via the photoelectric effect that can compensate space charges. Details on the plasma in the WGTS can e.g. be found in [KH+18].

Activity monitoring: β electrons either arrive at the detector or hit the wall of the experiment. A super conducting coil ensures that the magnetic flux tube terminates at the rear wall. On that account, most β electrons (99.99 %) hit the rear wall where they emit bremsstrahlung. Two dedicated beta-induced X-ray spectroscopy (BIXS) systems measure the corresponding X-ray spectrum to determine the source strength respectively the gas column density (2.1).

2.2.3. Differential Pumping Section

The differential pumping section (DPS) is an approximately 5 m-long cryostat. It is depicted in figure 2.4 and a detailed description can e.g. be found in [Kos12]. In short, it fulfills the following tasks:

Reduction of tritium flow: The differential pumping section (DPS) consists of 5 beam tube elements with pump ports between them. The beam tube elements form a 20° angle to each other and are arranged in a chicane. While β electrons are magnetically guided along the chicane, the neutral gas molecules scatter off the walls. This reduces the molecular beaming effect and enhances the pumping probability. Turbo molecular pumps then reduce

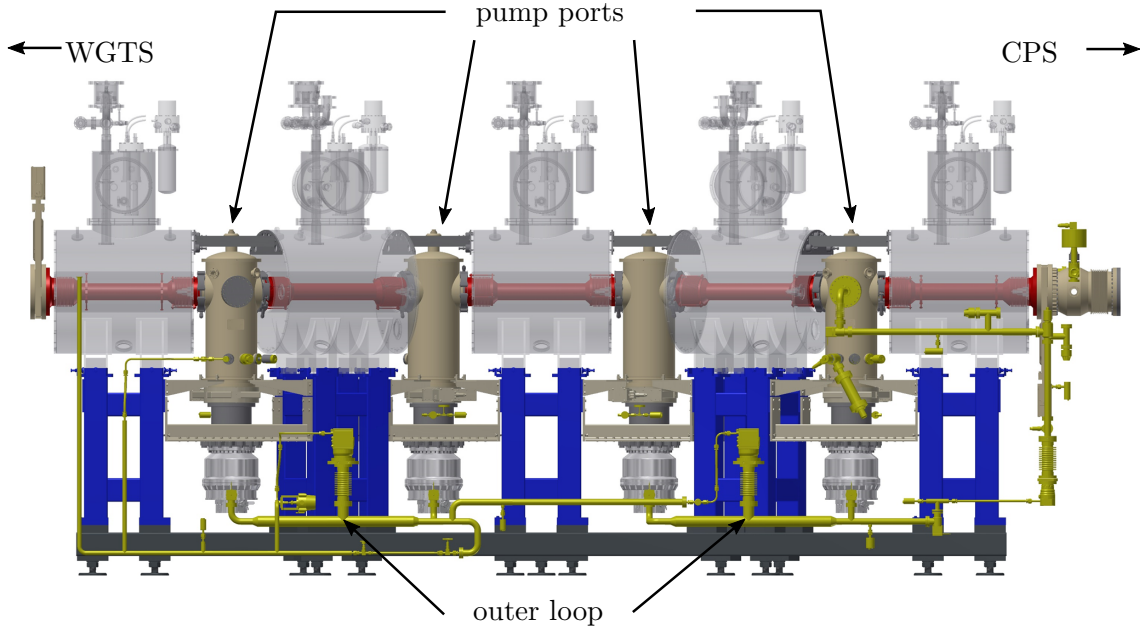


Figure 2.4.: The differential pumping section (DPS) reduces the gas flow and blocks tritium ions. (Adapted from [Sei19])

the gas flow by approximately 5 orders of magnitude and feed the gas into the so-called outer loop where it is reprocessed.

Ion blocking: In the WGTS ions such as HeT^+ , T_2^+ , T_3^+ , T_5^+ can form. If not blocked, they reach the spectrometer section analogously to the electrons which would eventually lead to an increased background rate. A potential barrier created by two ring electrodes set to +100 V avoids this. The positive ions are deflected, drift out of the flux tube, hit the wall and get neutralized.

Ion monitoring: Downstream of the blocking electrodes the remaining ion flux is measured by a Fourier transform ion cyclotron resonance device (FT-ICR). Details on ion forming and their measurement can e.g. be found in [UR+09].

2.2.4. Cryogenic Pumping Section

The cryogenic pumping section (CPS) is an approximately 7 m-long cryostat. It is depicted in figure 2.5 and a detailed description can e.g. be found in [Jan15]. In short, it fulfills the following tasks:

Reduction of tritium flow: The cryogenic pumping section (CPS) consists of 7 beam tube elements of which 5 are arranged in a similar manner as the beam tube elements of the differential pumping section (DPS) in a chicane forming 15° angles. While charged particles are guided along the chicane by a magnetic field, neutral molecules hit the wall. The walls are covered by a frozen argon layer cooled down to 3 K in order to cold-trap particles. After the accumulation of about 1 Ci of tritium the argon frost layer has to be renewed. To achieve this the beam tube is warmed-up and the argon is pumped off along with the accumulated tritium. Tests and simulations show a reduction of the tritium flow by approximately 10 orders of magnitude.

The forward beam monitor (FBM): The FBM is a detector that can be moved horizontally into the pump port of the CPS with a 2-dimensional spacial resolution of

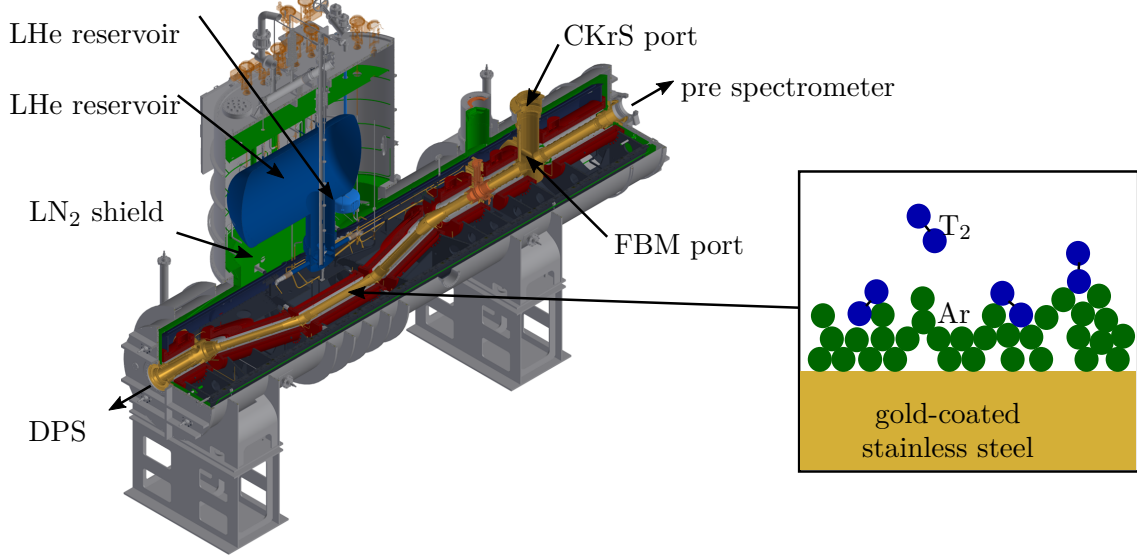


Figure 2.5.: The cryogenic pumping section (CPS) is the coldest part of the KATRIN experiment. Parts of its beam tube are covered by a frozen argon layer at 3 K to cold-trap tritium molecules. The low temperatures are established using liquid helium (LHe) and an insulation of liquid nitrogen (LN₂). (Adapted from [Sei19])

0.1 mm. Two pin-diodes measure the β electron flux and hence, the stability of the column density (2.1). Furthermore, the forward beam monitor (FBM) equips a temperature and a hall sensor. A second detector board holding a Faraday cup for ion measurements is also available. Details on the FBM can e.g. be found in [EH+17].

The condensed ^{83m}Kr source (CKrS) is a sub mono-layer of ^{83m}Kr on a pyrolytic graphite substrate with a diameter of 2 cm. It can be lowered in the pump port of the CPS and moved in a 2-dimensional plane perpendicular to the beam line. This enables the spacial scanning of the properties of the spectrometer using quasi-monoenergetic conversion electron lines of ^{83m}Kr . Details on the CKrS can e.g. be found in [Bau14].

2.2.5. Pre and Main Spectrometer

The pre and main spectrometer are vacuum vessels designed to filter passing electrons according to their kinetic energy. The pre spectrometer has a length of 3.4 m and a diameter of 1.7 m. Details on its design can e.g. be found in [PR+12]. The main spectrometer has a length of 23 m and a diameter of 10 m. Details on its design can e.g. be found in [Ang+05].

Magnetic adiabatic collimation with electrostatic filtering (MAC-E): The pre and main spectrometer apply the so-called MAC-E principle. A retarding voltage deflects electrons with insufficient kinetic energy. The electric field gradient is parallel to the beam line, but β electrons might be emitted in an arbitrary angle. In order to analyze their full kinetic energy they have to be collimated. This is done by a magnetic field gradient. A quantitative description of this process can be found in section 2.3. The precision of the MAC-E principle increases with the size of the spectrometer. That is why the main spectrometer of KATRIN has a larger diameter (10 m) as the ones of its predecessor experiments.

Magnetic field: The main spectrometer is surrounded by a system of coils that creates the MAC-E filter's magnetic field. Upstream, there is the PS2 magnet; downstream the pinch as well as the detector magnet, which are superconducting solenoids. Their field is fine-tuned by a system of air coils around the spectrometer hull. There is the earth

magnetic field compensation system (EMCS) with coils parallel and perpendicular to the beam line axis. Furthermore, there is the low-field correction system (LFCS) with coils perpendicular to the beam line axis. The combined system constrains the electrons' flux tube to the spectrometer vessel and compensates the earth's magnetic field as well as effects from ferromagnetic materials in the spectrometer's surroundings. Details on the magnetic field settings can e.g. be found in [EB+18]. Additionally, a vertical and radial magnetic measuring system (VMMS and RMMS) are installed. The field inside the spectrometer vessel is assessed via samples of these measuring systems combined with simulations. Details on the VMMS and the RMMS can e.g. be found in [LH+18].

Electric field: A high voltage system establishes the MAC-E filter's retarding potential. According to the KATRIN Design Report [Ang+05] the retarding voltage's fluctuations must have a standard deviation smaller than 60 mV for the envisaged sensitivity on the neutrino mass. The antenna-like beam line setup is sensitive to electromagnetic fluctuations, which is why an active so-called post-regulation system is deployed. It monitors the retarding potential and regulates it with the needed precision. For the monitoring exist the so-called monitor spectrometer and a voltage divider. Details on the voltage calibration with the voltage divider can e.g. be found in [TM+09]. The monitor spectrometer is part of a second beam line in a separate building. Its retarding potential follows the one of the main spectrometer and is measured via ^{83m}Kr conversion lines. Details on the monitor spectrometer can be e.g. be found in [EB+14].

Background: According to the KATRIN Design Report [Ang+05] the electron rate of uncontrollable sources (background) must be less than 10 mHz. Several background-related aspects are:

Vacuum: The spectrometers are operated at a pressure on the order of 10×10^{-11} mbar to 10×10^{-12} mbar. This prevents electron scattering on residual gas and minimizes background effects by ionization. Correspondingly, several turbo molecular and getter pumps are installed at the spectrometer vessels. Furthermore, the spectrometers can be baked out at up to 350 °C. Details on the vacuum system can e.g. be found in [AB+16].

Wire electrodes: The inner walls of the spectrometer vessels are lined by wire electrodes. Their potential is at a few hundred volts below the spectrometer hull reflecting electrons coming from the vessel walls. These electrons might be induced by e.g. cosmic rays or emanate from the spectrometer wall. A detailed description of the wire electrodes can e.g. be found in [Val09].

Ion blocking: Analogously to the ones in the CPS (section 2.2.4), three blocking electrodes are installed; one between the CPS and the pre spectrometer, one between the pre and main spectrometer; and one between the main spectrometer and the detector.

Tandem setup: β electrons might scatter on residual gas or the beam line walls. This can either directly lead to secondary electrons or create positive ions that travel down the beam line. The positive ions in turn might again through scattering yield secondary electrons. The more β electrons enter the main spectrometer the higher is the probability to create secondary electrons. In order to reduce the flux of β electrons into the main spectrometer the retarding potential of the pre spectrometer is set to a few hundred volts below the one of the main spectrometer. On one hand this is a countermeasure against background events. But on the other hand, charged particles can be trapped between the two spectrometers due to the electromagnetic setup (Penning trap). A sudden discharge might harm the hardware, especially the detector. Therefore, it is possible to sweep a charged wire through the volume in order to collect the trapped particles and avoid this "Penning-discharges".

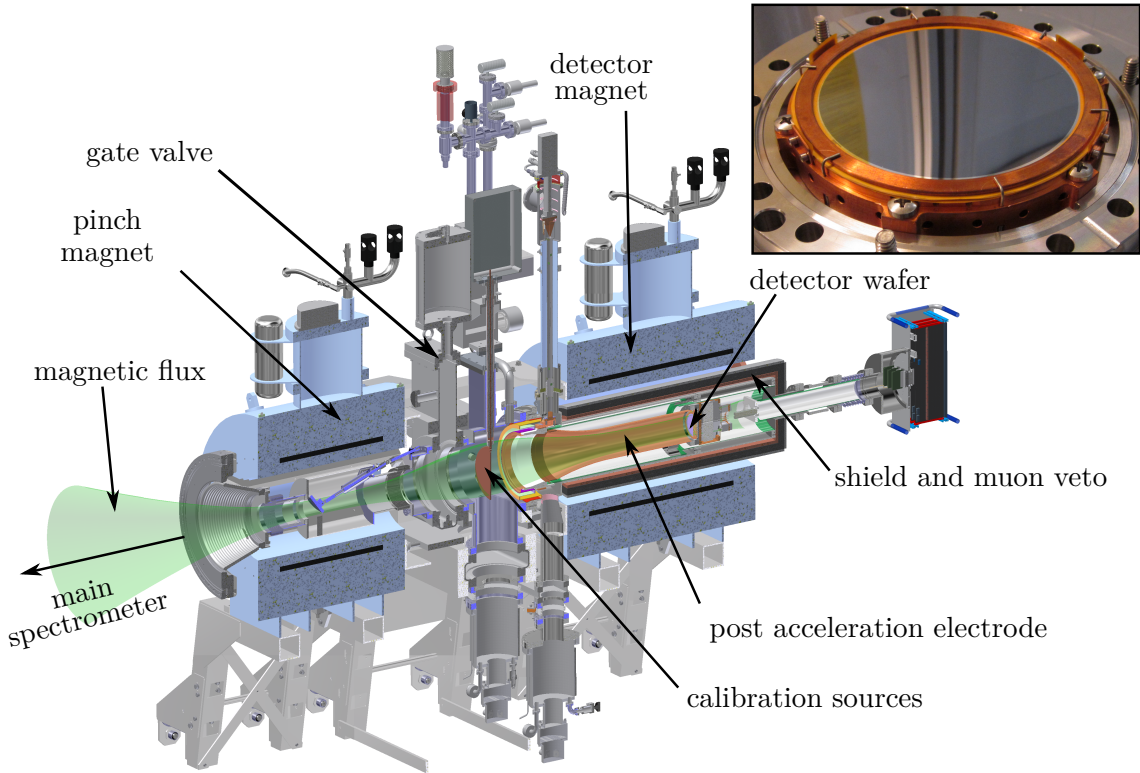


Figure 2.6.: The detector section terminates the KATRIN beam line. Among other instruments it houses the focal plane detector for β electrons with the detector wafer at its core.(Adapted from [Sei19])

2.2.6. Detector Section

The detector section terminates the beam line in downstream direction. It can be separated from the spectrometer section by closing a gate valve. The detector section is depicted in figure 2.6 and a detailed description can e.g. be found in [AB+15].

The focal plane detector (FPD) counts the β electrons that pass the spectrometer section. The FPD is a pin-silicon detector with a sensitive area of 9 cm diameter. It is subdivided in 148 pixels of the same area arranged in 12 rings of 12 pixels each and the so called bull's eye of 4 pixels in the center. This arrangement allows later correction for radial electrical and magnetic inhomogeneities in the beam line.

Shield and veto system: The FPD system's radiation shield consists of two nested cylindrical shells: an outer lead shell of 3 cm that reduces photon background and an inner copper shell of 1.27 cm that blocks X-rays originating from the outer lead shell. The shield is surrounded by a veto system to tag incoming muons.

Calibration: Photoelectron sources can be lowered in the detectors line of sight. The corresponding photocurrent can be measured with the so-called precision ultra-low current integrating normalization electrometer for low-level analysis (PULCINELLA) system. A comparison of PULCINELLA and the FPD yields the FPD's detection efficiency.

The detector magnet allows to form the flux tube near the detector independently of the main spectrometer magnetic field setting. This is especially useful in the above mentioned calibration process.

The post-acceleration electrode allows to shift the energy of β electrons arriving from the main spectrometer. This way β electrons can be distinguished from background

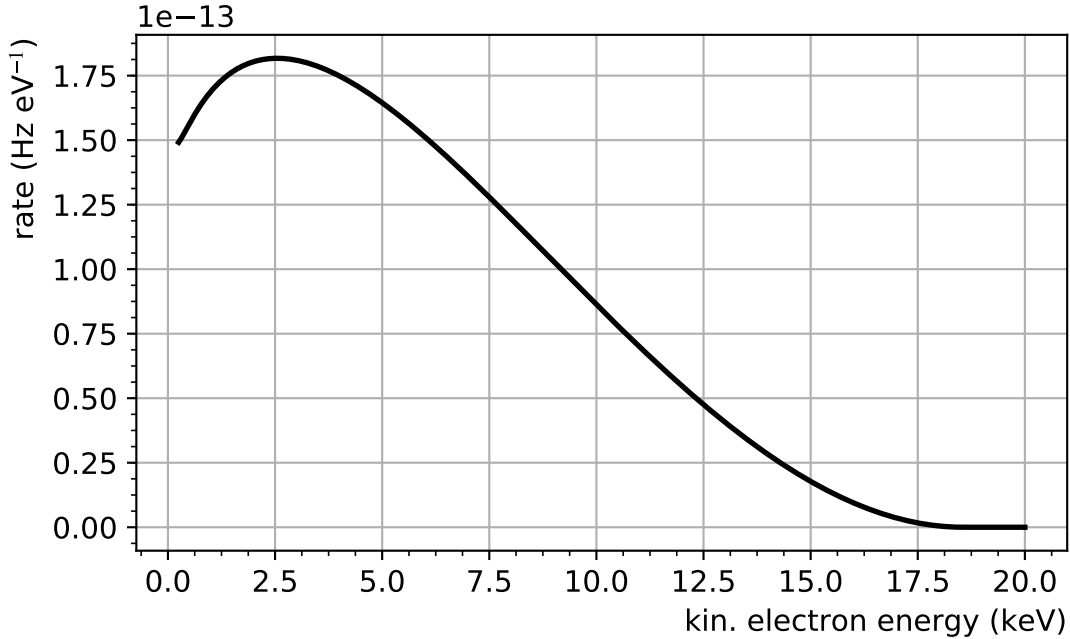


Figure 2.7.: The β decay spectrum of a tritium molecule as calculated by SSC.

electrons originating in the detector section by an energy region of interest cut.

2.3. Modelling of the Integrated β Decay Spectrum with SSC

An analytic description for the electron rate measured by the FPD can be derived. The derivation mostly follows [KB+19; Gro15; Kle14] or is extracted from current production code [KAT19]. The formulas are implemented in the so-called source and spectrum calculation (SSC) software framework.

2.3.1. β Decay Spectrum

In β^- decay the released energy is distributed among the emitted electron and the anti-electron neutrino. The differential decay rate of a tritium molecule can be described using Fermi theory and Fermi's golden rule as

$$\left(\frac{d\Gamma}{dE} \right) = \frac{G_F^2 |V_{ud}|^2}{2\pi^3} |M_{\text{nuc}}|^2 \cdot F(Z, E) \cdot p(E + m_e) \cdot \sum_{f,i} P_f |U_{ei}|^2 \epsilon_f \sqrt{\epsilon_f^2 - m_i^2} \cdot \Theta(\epsilon_f - m_i) \quad (2.3)$$

It is depicted in figure 2.7. Its constituents are the kinetic electron energy E ; the PMNS matrix U (1.4); the neutrino eigenmasses m_i (1.12); the Fermi constant G_F ; the up-down-quark-coupling given by the Cabibo angle θ_C

$$V_{ud} = \cos \theta_C = 0.97425 \pm 0.00022; \quad (2.4)$$

and the nuclear transition matrix element

$$M_{\text{nuc}} = g_V^2 + 3g_A^2 \quad \text{with } g_V = 1 \quad \text{and} \quad g_A/g_V = -1.2646 \pm 0.0035 \quad (2.5)$$

which is independent of the electron's kinetic energy as the decay is super-allowed and given by the vector g_V and axial vector g_A coupling.

Furthermore, the Fermi function $F(Z, E)$ accounts for the Coulomb interaction between the outgoing electron and the daughter nucleus with atomic charge $Z = 2$ which in its relativistic version can be approximated as

$$F(Z, E) \approx \frac{2\pi\eta}{1 - \exp 2\pi\eta} \cdot R \quad (2.6)$$

with Sommerfeld parameter $\eta = \alpha Z/\beta$, fine structure constant α , relativistic velocity β and a relativistic correction factor $R = 1.002037 - 0.001427\beta$.

The phase-space factor of the outgoing electron with momentum p and mass m_e is given by the factor $p(E + m_e)$.

The phase space factor of the emitted neutrino is described in dependence of the following quantities: total nuclear tritium decay energy Q (mass difference of mother and daughter nucleus) corrected for the nucleus recoil E_{rec} also called endpoint of the β spectrum

$$E_0 = Q - E_{\text{rec}}; \quad (2.7)$$

the kinetic electron energy E and the final state energy of the molecular system V_f . The probability that the molecular system is in a final state of energy V_f after the decay is denoted by P_f . Then the energy of the neutrino reads

$$\epsilon_f = E_0 - E - V_f. \quad (2.8)$$

The excited energy state f is caused by vibration, rotation or electronic excitation of the decaying molecule. Details and tabulated values can e.g. be found in [BPR15] and references therein.

The neutrino's momentum is $\sqrt{\epsilon_f^2 - m_i^2}$, where m_i denotes one of the neutrino eigenmasses. The complete phase space factor of the neutrino is a sum over all possible molecular final states labeled f and neutrino eigenmasses labeled i .

Lastly, the Heavyside step function Θ ensures a positive kinetic energy of the neutrino.

2.3.2. Detector Counts

The KATRIN detector counts electrons. The β electrons are adiabatically guided from the WGTS to the detector by magnetic fields. The magnetic field lines are parallel to the beam line axis. The angle between the flight direction of a β electron and the beam line axis towards the detector is denoted by the pitch angle $\theta \in [0^\circ, 180^\circ]$. The starting position of an β electron is denoted by its 1-dimensional coordinate along the beam line axis z_S .

KATRIN measures an integrated β spectrum. In other words, the detector counts electrons of kinetic energy E_S above a threshold, the so-called retarding energy qU . The integrated β spectrum can be scanned by varying qU .

A β electron emitted in the WGTS reaches the detector with a probability modeled by the so-called response function R (see section 2.3.7). R depends on the experimental settings (such as the electromagnetic fields and the gas dynamics) and especially on the retarding energy qU . Here, R denotes the transmission probability for a β electron of a fixed starting kinetic energy E_S , starting position z_S and starting pitch angle θ_S . The probability of a β electron for being counted when reaching the detector is denoted by the detection efficiency ϵ_{det} . Furthermore, the number of tritium molecules in the WGTS in a small area around the coordinate z is denoted by $dN_T(z)$.

Then, the measured integrated rate is expressed as integral from the threshold energy qU to the endpoint energy E_0 (2.7) over the differential rate $d\Gamma/dE_S$ (2.3) weighted with the probability given by R as

$$\Gamma(qU, z_S, \theta_S) = \epsilon_{\text{det}} \cdot dN_T(z_S) \cdot \int_{qU}^{E_0} \left(\frac{d\Gamma(E_S)}{dE_S} \right) \cdot R(E_S, qU, z_S, \theta_S) dE_S, \quad (2.9)$$

which eventually leads to β electron counts by multiplication with the measurement time $t(qU)$ at a retarding energy qU

$$N(qU, z_S, \theta_S) = \Gamma(qU, z_S, \theta_S) \cdot t(qU). \quad (2.10)$$

2.3.3. Discretization of the WGTS Volume

The counts N (2.10) are given for β electrons of a fixed starting position z_S . All starting positions $z_S \in [-L/2, +L/2]$ within the WGTS of length L contribute to the total count rate at the detector. Integrating along the beam axis accounts for this

$$N(qU, \theta_S) = \int_{-L/2}^{+L/2} \frac{dN(qU, \theta_S, z_S)}{dz_S} dz_S \quad (2.11)$$

Numerically, the same result can be obtained by a sufficiently fine discretization of the WGTS volume into S slices. The counts N (2.10) are adapted accordingly to account for discrete starting β electron positions z_S^j

$$N(qU, \theta_S, z_S) \rightarrow N^j(qU, \theta_S, z_S^j) \equiv N^j(qU, \theta_S). \quad (2.12)$$

Then, the total counts read

$$N(qU, \theta_S) = \sum_{j=1}^S N^j(qU, \theta_S). \quad (2.13)$$

Within this chapter, from here forth all quantities that are subject to discretization will be labeled with an upper index j . The discretization especially propagates to the response function $R \rightarrow R^j$ and its constituents.

2.3.4. Magnetic Bottle Effect

The β electrons are adiabatically guided to the detector by magnetic fields. The magnetic field strength at the starting position of a β electron in the WGTS is denoted by B_S^j . The maximum magnetic field strength along the beam line is denoted by B_{\max} . As $B_S^j < B_{\max}$ β electrons travelling downstream to the detector are subject to the magnetic bottle effect. They get reflected and travel upstream to the rear wall if their starting pitch angle θ_S surpasses θ_{\max}^j with

$$\sin \theta_{\max}^j = \sqrt{\frac{B_S^j}{B_{\max}}}. \quad (2.14)$$

(Its KATRIN design value is $\theta_{\max} \approx 51^\circ$.) A cutting angle θ_{\max}^j is beneficial because the greater the emission angle of a β electron the larger the distance it travels in the WGTS and the more it is subject to energy losses such as scattering or synchrotron radiation.

2.3.5. Scattering Probabilities

The probability for a β electron to reach the detector (the response function R^j) depends on the scattering probabilities P_l ($l \in \mathbb{N}$). P_l denotes the probability of an electron to scatter l times when travelling through the WGTS. P_l depends on the starting position z_S of a β electron in the WGTS as well as on its starting pitch angle θ_S . The expected scattering count for a β electron when travelling through the WGTS is the product of the line density λ the electron passes through and the scattering cross section σ

$$\mu(z_S, \theta_S) = \lambda(z_S, \theta_S) \sigma. \quad (2.15)$$

The electron moves on a spiral due to its cyclotron motion. Therefore, when traveling an infinitesimal distance dz in z -direction, it travels a total distance of

$$ds = \frac{1}{\cos \theta_S} dz. \quad (2.16)$$

The line density λ can be expressed as a line integral over the gas density ρ along the electrons path φ

$$\lambda(z_S, \theta_S) = \int_{\varphi} \rho(\vec{r}) ds. \quad (2.17)$$

Assuming that the gas density ρ only depends on the z -position along the beam line and vanishes for $z > L/2$ (beyond the WGTS) equation (2.17) becomes

$$\lambda(z_S, \theta_S) = \frac{1}{\cos \theta_S} \int_{z_S}^{L/2} \rho(z) dz. \quad (2.18)$$

Hence, the expected scattering count (2.15) becomes

$$\mu(z_S, \theta_S) = \frac{\sigma}{\cos \theta_S} \int_{z_S}^{L/2} \rho(z) dz. \quad (2.19)$$

The scattering process fulfills the conditions of a Poisson process, namely scattering once does quasi not influence the probability of an electron to scatter again; the expected scattering count μ (2.19) stays quasi constant; and it is unlikely for two scatterings to happen within a short distance. Thus, the probability for l -fold scattering can be expressed as a Poisson distribution

$$P_l(z_S, \theta_S) = \frac{\mu(z_S, \theta_S)^l}{l!} e^{-\mu(z_S, \theta_S)}. \quad (2.20)$$

Discretization of the WGTS volume

In the discretized case the WGTS volume is divided into S slices indexed by k with an average gas density $\bar{\rho}^k$. A slice k starts at position Z_s^k and ends at position Z_e^k with a width of $W^k = Z_e^k - Z_s^k$. For β electrons that start at a position z within slice j the expected scattering count (2.15) becomes

$$\mu(z_S, \theta_S) \rightarrow \mu^j(z, \theta_S) = \underbrace{\frac{\sigma}{\cos \theta_S}}_{(*)} (Z_e^j - z) \underbrace{\bar{\rho}^j}_{(**)} \sum_{k=j+1}^S \bar{\rho}^k W^k. \quad (2.21)$$

The gas column density in front of a β electron is split in two parts: the slice of its origin (*) and all slices downstream (**).

The Poisson distribution is formed for the expected scattering count μ^j (2.21) and averaged over all starting positions within the slice j which yields the discretized scattering probabilities

$$P_l^j(\theta_S) = \frac{1}{W^j} \int_{Z_s^j}^{Z_e^j} \frac{(\mu^j(z, \theta_S))^l}{l!} e^{-\mu^j(z, \theta_S)} dz. \quad (2.22)$$

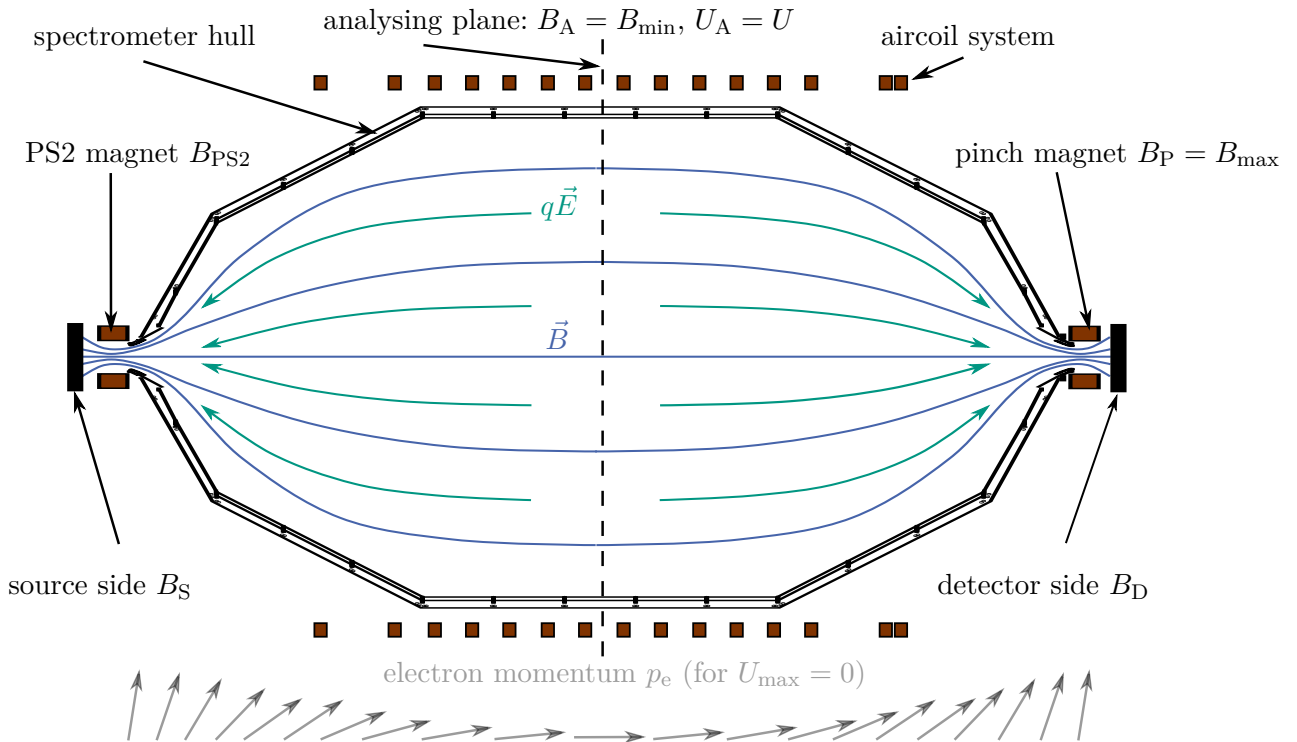


Figure 2.8.: Schematic of the KATRIN main spectrometer and the magnetic adiabatic collimation with electrostatic filtering (MAC-E) principle. The KATRIN design magnetic field settings are $B_{PS2} = 4.5$ T, $B_S^j = 3.6$ T, $B_{\max} = 6.0$ T, $B_D = 3.6$ T, $B_A \approx 3 \times 10^{-4}$ T. \vec{E} denotes the magnetic field regulated by the retarding potential U that reaches its maximum $U_a = U$ at the analyzing plane. (Adapted from [Sei19])

2.3.6. MAC-E Principle and Transmission Function

The spectrometers of KATRIN follow the magnetic adiabatic collimation with electrostatic filtering (MAC-E) principle. Figure 2.8 shows a corresponding sketch. The main spectrometer is a vacuum vessel with a downstream magnet of strength B_{PS2} and an upstream magnet of strength B_P making electrons form a magnetic flux tube. In the case of KATRIN the fluxtube begins in the STS with a magnetic field strength of B_S^j . In other words, the spectroscopic properties are not solely determined by the spectrometer vessel, but also by the STS. The minimum magnetic field strength $B_{\min} = B_A$ is reached at the so-called analyzing plane in the vessel center. Electrons entering the vessel perform cyclotron motions around the magnetic field lines. Their total kinetic energy E_S is split into a longitudinal component E_{\parallel} along the beam axis and a transverse component E_{\perp}

$$E_S = E_{\parallel} + E_{\perp}. \quad (2.23)$$

In the non-relativistic and adiabatic approximation the transverse component can be expressed by the magnetic field strength B and the electron's magnetic moment μ respectively its charge $q = e$, its mass m_e and angular momentum L .

$$E_{\perp} = -\mu B = \frac{e}{2m_e} LB. \quad (2.24)$$

Adiabaticity conserves angular momentum L and the total energy of the electron E_S . Hence, when the magnetic field strength B decreases to $B_A = B_{\min}$ in the analyzing plane, the transverse component of the electron's energy E_{\perp} decreases likewise and transforms to

longitudinal energy E_{\parallel} . Additionally, a retarding voltage barrier is applied along the beam axis, reaching its maximum U at the analyzing plane and dropping off towards the source and the detector. In order to pass through the filter, electrons need a total kinetic energy E_S greater than the transmission energy $E_{\text{tr}}^j(qU, E_S, \theta_S)$ that depends on their starting potential U_S^j , their starting pitch angle θ_S and starting Lorentz factor γ_S

$$E_{\text{tr}}^j(qU, E_S, \theta_S) = \frac{q(U - U_S^j)}{1 - \sin^2 \theta_S \frac{B_A}{B_S^j} \frac{\gamma_S + 1}{2}}. \quad (2.25)$$

For ease of notation, the dependency on B_S^j , B_A and U_S^j is left implicit. Note further that the right hand side of (2.25) also depends on the starting energy of a β electron as it depends on γ_S .

Then, the probability for an electron to pass through a MAC-E filter, the so-called transmission function, can be written as

$$\mathcal{T}^j(E_S, qU, \theta_S) = \begin{cases} 1 & \text{if } E_S > E_{\text{tr}}^j(qU, E_S, \theta_S) \\ 0 & \text{otherwise} \end{cases}. \quad (2.26)$$

The transmission condition for the energy $E_S > E_{\text{tr}}^j(qU, E_S, \theta_S)$ can be reformulated to a condition for the pitch angle θ_S^j

$$E_S > E_{\text{tr}}^j(qU, E_S, \theta_S) \quad (2.27)$$

$$\Leftrightarrow \theta_S < \theta_{\text{tr}}^j(E_S, qU) := \arcsin \left(\sqrt{\frac{E_S - q(U - U_S^j)}{E_S} \frac{B_A}{B_S^j} \frac{\gamma_S + 1}{2}} \right) \quad (2.28)$$

This allows to rewrite the transmission function (2.26) as

$$\mathcal{T}^j(E_S, qU, \theta_S) = \begin{cases} 1 & \text{if } \theta_S > \theta_{\text{tr}}^j(E_S, qU) \\ 0 & \text{otherwise} \end{cases}. \quad (2.29)$$

2.3.7. Response Function

The so-called response function denotes the probability of a β electron emitted in the WGTS with starting energy E_S and pitch angle θ_S to reach the detector when a retarding voltage of U is applied to the spectrometer. In addition to the transmission function \mathcal{T}^j (2.27) it incorporates the energy loss ϵ of the β electrons due to scattering in the gas in the WGTS. If up to N -fold scattering is considered, the response function reads

$$R^j(E_S, qU, \theta_S) = \int_0^{E_S} \sum_{l=1}^N \mathcal{T}^j(E_S - \epsilon, qU, \theta_S) \cdot P_l^j(\theta_S) \cdot f_l(\epsilon) d\epsilon. \quad (2.30)$$

Here, P_l^j (2.22) denotes the probability of a β electron to scatter l times when travelling through the WGTS. $f_l(\epsilon)$ is the so-called energy loss function. It denotes the probability for β electrons to lose the energy ϵ when scattering l times. For no scattering the Dirac delta function is used

$$f_0(\epsilon) = \delta(\epsilon). \quad (2.31)$$

For 1-fold scattering f_1 is denoted without index $f_1 = f$. For $l > 1$ and l -fold scattering f_l is the l -fold convolution of f with itself

$$f_l(\epsilon) = \bigotimes_{i=1}^l f(\epsilon) \quad (2.32)$$

where \otimes denotes the convolution

$$(f \otimes f)(\epsilon) = \int_0^\infty f(\epsilon - \epsilon') f(\epsilon') d\epsilon'. \quad (2.33)$$

2.3.8. Energy Loss Function

The response function (2.30) depends on the energy loss function f . $f(\epsilon)$ denotes the probability of a β electron to loose the energy ϵ when scattering once on a gas molecule. A review of different models for f can e.g. be found in [Tro19]. E.g. a phenomenological model fitted to data was established by the Troitsk experiment for tritium [AB+00] as well as for deuterium and hydrogen molecules [AB17]. Currently a corresponding modeling effort is made based on data taken by KATRIN. Details will be discussed in section ??.

2.3.9. Distribution of Pitch Angles

The detected counts N (2.13) are given for a fixed starting pitch angle θ_S of β electrons which motivates to average over pitch angles. Any function $g(\theta_S)$ depending on a fixed pitch angle θ_S can be averaged given the distribution $\omega(\theta_S)$ of θ_S and its maximum value θ_{\max}^j (2.14) as

$$\langle g(\theta_S) \rangle \equiv \bar{g} = \frac{\int_0^{\theta_{\max}^j} \omega(\theta_S) g(\theta_S) d\theta_S}{\int_0^{\theta_{\max}^j} \omega(\theta_S) d\theta_S}. \quad (2.34)$$

An isotropic β electron emission by a tritium molecule into the unit sphere, meaning all combinations of spherical emission angles $(\varphi, \vartheta = \theta_S)$ are equally likely, yields as distribution for their starting pitch angle

$$\omega(\theta_S) = \sin \theta_S \quad (2.35)$$

$$\int_0^{\theta_{\max}^j} \omega(\theta_S) d\theta_S = \frac{1}{1 - \cos \theta_{\max}^j}. \quad (2.36)$$

Scattering Probabilities

Averaging the scattering probabilities P_l^j (2.22) yields

$$\bar{P}_l^j = \frac{1}{1 - \cos \theta_{\max}^j} \int_0^{\theta_{\max}^j} P_l^j(\theta_S) \sin \theta_S d\theta_S. \quad (2.37)$$

This expression is helpful when averaging the detected counts N (2.13) and bringing the corresponding averaged response function in a demonstrative form as shown below.

Counts and Response Function

The detected counts N (2.13) depend on the starting pitch angle θ_S of the β electrons. They have to be averaged over θ_S . The corresponding integral can be swapped with the sum over the WGTS slices and the integral over the energy and propagates to the response term

$$\bar{N}(qU) \propto \sum_{j=1}^S N_T^j \int_{qU}^{E_0} \left(\frac{d\Gamma(E_S)}{dE_S} \right) \cdot \frac{1}{1 - \cos \theta_{\max}^j} \int_0^{\theta_{\max}^j} R^j(E_S, qU, \theta_S) \sin \theta_S d\theta_S dE_S. \quad (2.38)$$

Here N_T^j denotes the number of tritium molecules in a WGTS slice j . The response function R^j (2.30) can be averaged as

$$\begin{aligned} \bar{R}^j(E_S, qU) &= \frac{1}{1 - \cos \theta_{\max}^j} \int_0^{\theta_{\max}^j} R^j(E_S, qU, \theta_S) \sin \theta_S d\theta_S \\ &= \int_0^{E_S} \sum_{l=1}^N \frac{1}{1 - \cos \theta_{\max}^j} \int_0^{\theta_{\max}^j} \mathcal{T}^j(E_S - \epsilon, qU, \theta_S) \cdot P_l^j(\theta_S) \sin \theta_S d\theta_S f_l(\epsilon) d\epsilon. \end{aligned} \quad (2.39)$$

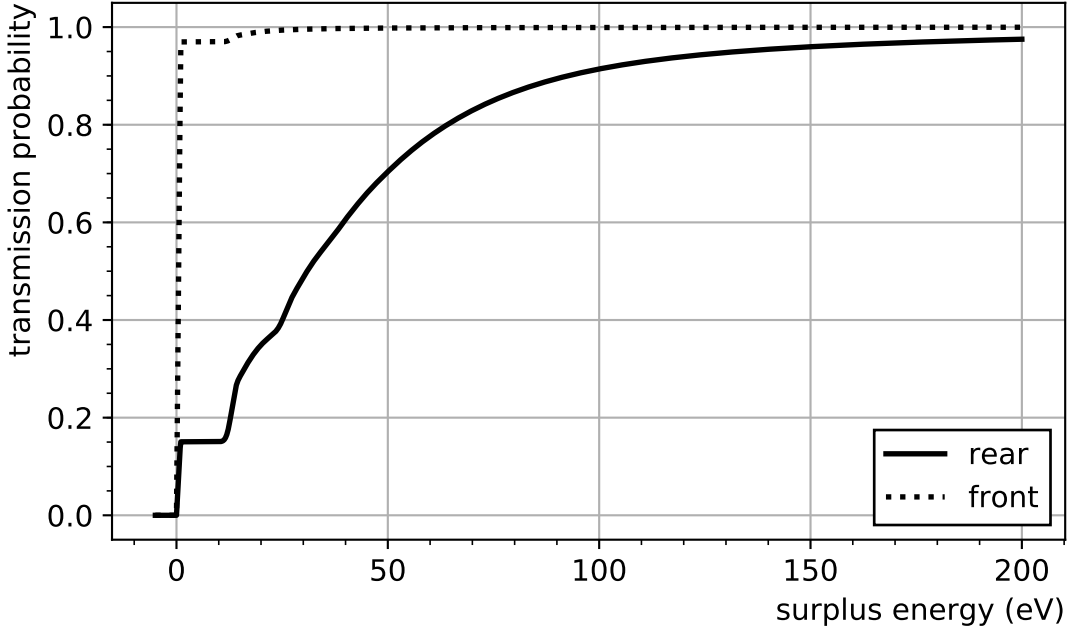


Figure 2.9.: The response function as calculated by SSC. The surplus energy denotes the difference between the starting kinetic energy E_S of a β electron and the retarding energy qU . The response function \bar{R}^j (2.42) is depicted for electrons starting at the rear and front of the WGTS.

The transmission function \mathcal{T}^j (2.29) is a step function. Assuming that θ_{\max}^j (2.14) is always greater than the transmission angle θ_{tr}^j (2.27), the upper integral boundary changes which yields the averaged response function

$$\bar{R}^j(E_S, qU) = \int_0^{E_S} \sum_{l=1}^N \int_0^{\theta_{\text{tr}}^j(E_S - \epsilon, qU)} \frac{\sin \theta_S \cdot P_l^j(\theta_S)}{1 - \cos \theta_{\max}^j} d\theta_S f_l(\epsilon) d\epsilon. \quad (2.40)$$

The averaged response function \bar{R}^j is depicted in figure 2.9. Its formula (2.40) can be rewritten to match the form of the formula for the non-averaged response function R^j (2.30). Therefore, the averaged scattering probabilities \bar{P}_l^j (2.37) are used and the factor $1 = \bar{P}_l^j / \bar{P}_l^j$ is inserted in equation (2.40):

$$\bar{R}^j(E_S, qU) = \int_0^{E_S} \underbrace{\sum_{l=1}^N \int_0^{\theta_{\text{tr}}^j(E_S - \epsilon, qU)} \frac{\sin \theta_S \cdot P_l^j(\theta_S)}{(1 - \cos \theta_{\max}^j) \cdot \bar{P}_l^j} d\theta_S \cdot \bar{P}_l^j \cdot f_l(\epsilon) d\epsilon}_{T^{j,*}(E_S - \epsilon, qU)} \quad (2.41)$$

$$= \int_0^{E_S} \sum_{l=1}^N T^{j,*}(E_S - \epsilon, qU) \cdot \bar{P}_l^j \cdot f_l(\epsilon) d\epsilon. \quad (2.42)$$

Note that the non-averaged response function R^j (2.30) has the same form as the averaged one \bar{R}^j (2.42) if the non-averaged transmission function \mathcal{T}^j (2.29) is replaced by the modified transmission function $T^{j,*}$ and the non-averaged scattering probabilities P_l^j (2.20) by the averaged ones \bar{P}_l^j (2.37).

Note further that albeit equation (2.40) and equation (2.42) are analytically equal, they are not equal implementation-wise. Currently the implementation of the response function follows equation (2.42). On one hand, equation (2.40) is more “light-weight” as it does not use the averaged scattering probabilities. In the future it might be beneficial to alter the

implementation to simplify the program structure and cut down on the number of calculations. On the other hand, equation (2.41) allows the exchange of implementations for the transmission function whereas equation (2.40) only allows to exchange the implementation of the response function as a whole.

2.3.10. Reconciliation

The predicted counts for a retarding energy of qU when measuring a duration $t(qU)$ are

$$\bar{N}(qU) = t(qU) \cdot \epsilon_{\text{det}} \cdot \left(A_S \cdot \sum_j N_T^j \cdot \int_{qU}^{E_0} \left(\frac{d\Gamma(E_S)}{dE_S} \right) \cdot \bar{R}^j(E_S, qU) dE_S + R_{\text{bg}} \right). \quad (2.43)$$

Here, $A_S = 1$ is a normalization factor, $\epsilon_{\text{det}} \in [0, 1]$ the detector efficiency, the sum goes over all source slices, N_T^j is the number of tritium molecules in the j th source slice, $(d\Gamma(E_S)/dE_S)$ is the differential rate from (2.3), $\bar{R}^j(E_S, qU)$ is the response function from (2.42) and R_{bg} is the rate of background events.

2.3.11. Amendments

Equation (2.43) is a scaffold for an analytic model of the counts measured by the KATRIN detector. Modifications of isolated terms can consider further effects. Selected examples are:

- **Doppler effect:** Gas flow and temperature move the tritium molecules and hence, smear the kinetic energy distribution of β electrons. This can be modelled by convolving the differential rate $d\Gamma/dE$ (2.3) with a Maxwellian distribution or by applying corrections to the final energy states of the decaying molecules.
- **Plasma potential:** Space charges, respectively a plasma, forms within the WGTS due to the tritium decay. Electrons passing through space charges might either gain or lose energy. In a segmented WGTS volume, this is implemented by using an effective retarding energy corrected for the plasma potential V^j in the slice j

$$qU \rightarrow qU_{\text{eff}}^j = qU - V^j \quad (2.44)$$

when calculating the response function \bar{R}^j (2.42). Note that this is equivalent to using the starting potential U_S^j in the transmission energy E_{tr}^j (2.25).

- **Further discretization of the WGTS volume:** The SSC software allows to discretize the WGTS not only into slices, but also to subdivide the slices further into rings and the rings into segments. This enables an arbitrary spacial binning for WGTS properties such as the magnetic field or gas density. Then, additionally, the retarding energy $qU \rightarrow qU^j$, the maximum magnetic field strength along the beam line $B_{\max} \rightarrow B_{\max}^j$, the magnetic field strength in the analyzing plane $B_A \rightarrow B_A^j$ and the detector efficiency $\epsilon_{\text{det}} \rightarrow \epsilon_{\text{det}}^j$ become subject to discretization because they exhibit a radial dependency. Furthermore, the WGTS can be subdivided into volumes that map onto a specific detector pixel due to magentic guidance. This enables pixel-wise modelling of electron counts.

2.4. A KATRIN Neutrino Mass Measurement

KATRIN measures electron counts as described in (2.43) at a set of retarding energies qU_i . How much measurement time $t(qU_i)$ is attributed to a certain retarding energy is called a measurement time distribution (MTD). The MTD influences the experiment's sensitivity to the neutrino mass. An optimal MTD balances the following aspects:

ToDo

1. Some measurement time has to be attributed to retarding energies beyond the endpoint of the spectrum to determine the background rate. The optimal duration depends on the background rate.
2. The shape of the integral tritium β spectrum depends the strongest on the neutrino mass near its endpoint E_0 (2.7). [\[Ask Hendrik for plot.\]](#)
3. Measurements deeper into the spectrum increase the count rate and hence, lower the statistical uncertainty due to Poisson statistics.
4. The theoretical description of the integral tritium β spectrum is optimized for the endpoint region. Deeper scans introduce modeling uncertainties.

The KATRIN Design Report [Ang+05] suggests 5 MTDs for different measurement ranges $[E_0 - \alpha \text{ eV}, E_0 + 5 \text{ eV}]$ with $\alpha \in \{20, 25, 30, 40, 50\}$ and the conclusion that $\alpha = 30$ yields the best sensitivity.

Furthermore, searches for sterile neutrinos at the keV-scale would require deeper scans. Also, during commissioning measurement it makes sense to vary the MTD, especially to perform deeper scans, to ensure a comprehensive understanding of the KATRIN apparatus.

Several measurement campaigns were already conducted. The First Tritium (FT) commissioning campaign successfully proved the apparatus functioning. The corresponding MTD covered a range starting at $\sim E_0 - 1.6 \text{ keV}$. The KATRIN Neutrino Mass Measurement 1 (KNM1) campaign is evaluated during the writing of this thesis. It set out to establish an unprecedented limit on the neutrino mass by β decay measurements. Its MTD starts at $\sim E_0 - 90 \text{ eV}$.

3. Parameter Inference at KATRIN with KaFit

3.1. Introduction

The neutrino mass m_ν , alongside with an uncertainty will be retrieved by comparing the output of the KATRIN measurement with theoretical predictions. This process is called parameter inference. There exist different statistical approaches. They differ in practicality as well as interpretation. The so-called KaFit software framework implements several corresponding tools tailored to the KATRIN experiment. It is interfaced to SSC (section 2.3). A description of KaFit can e.g. be found in [Kle14]. This chapter outlines a selection of statistical approaches following mainly the statistics chapter of the Review of Particle Physics [Tan+18]. Additionally, within this thesis the implementations in KaFit were extended, which will also be described.

3.2. The KATRIN Likelihood

The likelihood is the probability of a measurement outcome given a hypothesis. A hypothesis depending on a parameter vector $\boldsymbol{\theta}$ is called a composite hypothesis. A measurement outcome can be quantified by a vector of observed values \mathbf{x} . The probability P of \mathbf{x} given a hypothesis in dependence of $\boldsymbol{\theta}$ is called the likelihood function

$$L(\boldsymbol{\theta}) = P(\mathbf{x} \mid \boldsymbol{\theta}). \quad (3.1)$$

If p denotes the probability for one observed value x_i in \mathbf{x} , then the likelihood function can be written as a product

$$L(\boldsymbol{\theta}) = \prod_i p(x_i \mid \boldsymbol{\theta}). \quad (3.2)$$

The parameter vector $\hat{\boldsymbol{\theta}}$ that maximizes the likelihood function is called the maximum likelihood estimator (MLE) for the true values of $\boldsymbol{\theta}$.

The MLE-method can be applied to a KATRIN measurement as follows: The data vector is given by a set of n electron counts $\{N_{\text{obs},i}\}$ measured at different retarding potentials qU_i . The hypothesis is that these counts follow a Poisson distribution with predicted expected electron counts $\{N_{\text{theo},i}\}$ as e.g. in (2.43). For sufficiently high counts the Poisson distribution can be approximated by a Gaussian distribution $\mathcal{N}(x, \mu, \sigma)$ with mean $\mu = N_{\text{theo},i}(\boldsymbol{\theta})$ and standard deviation $\sigma = \sqrt{N_{\text{obs},i}}$. The likelihood function then reads

$$L(\boldsymbol{\theta}) = \prod_i^n \mathcal{N}\left(N_{\text{obs},i}, \mu = N_{\text{theo},i}(\boldsymbol{\theta}), \sigma = \sqrt{N_{\text{obs},i}}\right). \quad (3.3)$$

Commonly, instead of maximizing the likelihood function, its negative logarithm is minimized and a factor 2 is introduced

$$-2 \ln L(\boldsymbol{\theta}) = \chi^2(\boldsymbol{\theta}) = \sum_i^n \left(\frac{N_{\text{obs},i} - N_{\text{theo},i}(\boldsymbol{\theta})}{\sqrt{N_{\text{obs},i}}} \right)^2 + \text{constants}. \quad (3.4)$$

Under the made assumptions this so-called chi-square function follows the Pearson's chi-square statistic. Its minimization yields the MLE estimator $\hat{\boldsymbol{\theta}}$ for $\boldsymbol{\theta}$. Accordingly, the value $\chi^2(\hat{\boldsymbol{\theta}})$ is a measure for the goodness-of-fit.

The parameter of interest in $\boldsymbol{\theta}$ is the neutrino mass squared m_ν^2 . Furthermore, $\boldsymbol{\theta}$ typically comprises the endpoint of the tritium β spectrum E_0 (2.7), an overall normalization factor for the counts A_S and the rate of the background counts R_{bg} . For the later two see (2.43).

3.3. Intervals

The presented maximum likelihood method provides point estimates $\hat{\boldsymbol{\theta}}$. However, additional information can be provided by interval estimates. There are two main approaches to statistical inference, which may be called Bayesian and frequentist. They differ in their interpretation of probability which becomes especially evident by the interval estimates typically associated with the two approaches.

3.3.1. Bayesian Credible Intervals

The likelihood $L(\mathbf{x} | \boldsymbol{\theta})$ is a probability distribution of the data \mathbf{x} given the parameters $\boldsymbol{\theta}$. Using Bayes theorem, the likelihood can be transformed into a probability density for the parameters $\boldsymbol{\theta}$ by multiplication with a prior distribution $\pi(\boldsymbol{\theta})$ and normalization to 1

$$P(\boldsymbol{\theta} | \mathbf{x}) = \frac{L(\mathbf{x} | \boldsymbol{\theta})\pi(\boldsymbol{\theta})}{\int L(\mathbf{x} | \boldsymbol{\theta}')\pi(\boldsymbol{\theta}') d\boldsymbol{\theta}'} . \quad (3.5)$$

Here, $P(\boldsymbol{\theta} | \mathbf{x})$ is the so-called posterior distribution. So-called credible regions, in which the true parameters lie with a certain probability α , can be extracted. Typical values for α are 68 % and 95 %. When $\boldsymbol{\theta}$ is one dimensional a credible region becomes a credible interval.

3.3.2. Frequentist Confidence Intervals

In frequentist statistics, probability is interpreted as the frequency of the outcome of a repeatable experiment. A confidence region $C(\alpha)$ of confidence level (CL) α for a parameter vector with true value $\boldsymbol{\theta}_T$ is the following: If an experiment were to be repeated many times and the confidence region $C(\alpha)$ were to be constructed each time according to the same recipe, it would contain the true parameter $\boldsymbol{\theta}_T$ a fraction of at least α times. Typical values for α are chosen as quantiles of the Gaussian distribution in steps of standard deviations σ . E.g. the 1- and 2- σ levels are 68 % and 95 %. The Neyman construction [Ney37] or its extension, the unified approach by Feldman and Cousins [FC98], yield such confidence regions. When $\boldsymbol{\theta}$ is one dimensional a confidence region becomes a confidence interval.

Approximated confidence regions can be extracted from the likelihood. If the likelihood follows the form of a multivariate Gaussian distribution in $\boldsymbol{\theta}$, then the hyper surface defined by

$$\ln L(\boldsymbol{\theta}) = \ln L(\hat{\boldsymbol{\theta}}) - \frac{s^2}{2} \quad (3.6)$$

encloses a s - σ confidence region for $\boldsymbol{\theta}$. This is the case for the KATRIN chi-square likelihood.

3.4. Likelihood Extensions

The likelihood $L(\boldsymbol{\theta})$ can be multiplied by a function $g(\boldsymbol{\theta})$

$$-2 \ln L'(\boldsymbol{\theta}) = -2 \ln L(\boldsymbol{\theta}) - 2 \ln g(\boldsymbol{\theta}) . \quad (3.7)$$

This procedure may have different interpretations and usage scenarios. E.g. a comparison with (3.5) shows, if g is a prior probability distribution, L' becomes a non-normalized posterior distribution that can be used in a Bayesian analysis. A further interpretation is given in section 3.4.2.

3.4.1. Implementation

KaFit allowed to choose g in 3.7 as a product of one-dimensional Gaussian distributions. Within this thesis the software was extended to allow products of other functions. Three function types were explicitly made available through a configuration file.

1. A reimplementation of a one-dimensional Gaussian distribution: The reimplementation was necessary to conveniently enable the combination of function types.
2. A multivariate Gaussian distribution: This enables the treatment of uncertainties quantified by calibration or monitor measurements as described in section 3.4.2. It can also be used as a prior distribution in a Bayesian analysis. Particularly, correlations can be respected.
3. A one-dimensional probability density, that is constant in the square root of a parameter, if it is positive and 0 otherwise:

$$g(\theta) = \begin{cases} 0 & \text{if } \theta \leq 0 \\ \text{constant} \cdot \frac{1}{\sqrt{\theta}} & \text{if } \theta > 0 \end{cases}. \quad (3.8)$$

This can be used as a uniform prior on the neutrino mass ($\theta = m_\nu^2$). Formerly, it was only possible to use a uniform prior on the squared neutrino mass.

An example on how to configure KaFit using the new feature is given in appendix [\[Add ToDo appendix\]](#).

3.4.2. Combination of Measurements

If two measurements share a set of parameters $\boldsymbol{\theta}_s$, but have additionally an individual set of parameters $\boldsymbol{\theta}_1$ and $\boldsymbol{\theta}_2$ and different sets of observations a combined likelihood is given by the product of the single likelihoods L_1 and L_2

$$-2 \ln L(\boldsymbol{\theta}_s, \boldsymbol{\theta}_1, \boldsymbol{\theta}_2) = -2 \ln L_1(\boldsymbol{\theta}_s, \boldsymbol{\theta}_1) - 2 \ln L_2(\boldsymbol{\theta}_s, \boldsymbol{\theta}_2). \quad (3.9)$$

In the case of KATRIN the first measurement could be sensitive to the neutrino mass whereas say the second measurement could have been a calibration using the electron gun and be sensitive to parameters of the response function (2.42). Combining both likelihoods would incorporate the uncertainties on the parameters of the response function in the neutrino mass determination. Currently, no software framework exists that allows the construction of combined likelihoods of KATRIN neutrino mass and calibration measurements. Instead the following approximation can be made. The calibration measurement is evaluated independently and one obtains estimates $\hat{\boldsymbol{\theta}}_{s,2}$, and an estimated covariance matrix $\hat{V}_{s,2}$ for all components of $\boldsymbol{\theta}_s$ that the calibration measurement is sensitive to. These can in turn be used to approximate the likelihood L_2 at least in the dimension of $\boldsymbol{\theta}_s$. A choice that stands to reason for the approximation of L_2 is a multivariate Gaussian distribution. For the purpose of parameter inference through minimization $-2 \ln L_2$ needs only to be accurately approximated around its minimum. The choice of a multivariate Gaussian distribution corresponds a symmetric approximation of $-\ln L_2$ around its minimum by a parabola. The KATRIN likelihood for a combination of a neutrino mass and a calibration measurement then reads

$$\begin{aligned} -2 \ln L(\boldsymbol{\theta}_s, \boldsymbol{\theta}_1, \boldsymbol{\theta}_2) &\approx -2 \ln L'(\boldsymbol{\theta}_s, \boldsymbol{\theta}_1) \\ &= \underbrace{\chi^2(\boldsymbol{\theta}_s, \boldsymbol{\theta}_1)}_{(1)} + \underbrace{(\boldsymbol{\theta}_s - \hat{\boldsymbol{\theta}}_{s,2})^\top \hat{V}_{s,2}^{-1} (\boldsymbol{\theta}_s - \hat{\boldsymbol{\theta}}_{s,2})}_{(2)} + \text{constants} \end{aligned} \quad (3.10)$$

Here, (1) is the chi-square expression (3.4) where the $\boldsymbol{\theta}_s$ and $\boldsymbol{\theta}_1$ can be written as one combined parameter vector $\boldsymbol{\theta}$ for a neutrino mass measurement. And (2) resembles the negative log likelihood of the calibration measurement approximated by a multivariate Gaussian distribution. Terms having a form like (2) are also sometimes called “pull terms” or “likelihood penalties”. In the minimization process they “pull” the parameters $\boldsymbol{\theta}_s$ towards $\hat{\boldsymbol{\theta}}_{s,2}$ respectively “penalize”/increase the negative log likelihood if $\boldsymbol{\theta}_s$ and $\hat{\boldsymbol{\theta}}_{s,2}$ differ.

Note that the maximum of the overall likelihood $-2 \ln L'$ might no longer follow the Pearson chi-square statistic and strictly speaking the measure for goodness-of-fit might get lost. However, the chi-square characteristics remain if the neutrino mass measurement, term (1), is not sensitive to the shared parameters: $d\chi^2(\boldsymbol{\theta}_s, \boldsymbol{\theta}_1)/d\boldsymbol{\theta}_s = 0$. Because then the MLE for the shared parameters will match the MLE by the calibration measurement $\hat{\boldsymbol{\theta}}_s = \hat{\boldsymbol{\theta}}_{s,2}$ and term (2) will be 0. For example, a standard KATRIN 3-year neutrino mass measurement is not sensitive to parameters of the energy loss function (2.30). Hence, adding a corresponding term (2) will not influence the chi-square characteristics. However, a standard KATRIN 3-year neutrino mass measurement is sensitive to the gas column density (2.1). Adding a corresponding term (2) from (a naturally more sensitive) monitoring measurement would alter the distribution of the chi-square values. [\[Add plot for bayesian sensitivity study on eloss and column density.\]](#)

ToDo

What does parameter inference mean? What does sensitivity on the neutrino mass mean? What is the likelihood? What is a Frequentist approach? What is a Bayesian approach?

3.5. Overview of Analysis Methods

What are the parameters of interest? What is run stacking? What is a uniform fit? Was the neutrino mass fixed? Which energy loss model/fsd binning/...? More general, which analysis configuration was used and why?

3.6. Inference Algorithms

3.6.1. Classical Minimizer

What algorithm is implemented in/interfaced to KaFit? What is MINUIT and MINOS? What are the pros and cons?

3.6.2. Markov-Chain-Monte-Carlo

What is a Markov-Chain-Monte-Carlo? What algorithm is implemented in/interfaced to KaFit? What are the pros and cons of the method? What are the pros and cons of the different implementations?

3.7. Treatment of Uncertainties

3.7.1. Nuisance Parameters

What are nuisance parameters? How can they be included in an analysis? What are the difficulties? How can these difficulties be circumvented?

3.7.2. Penalized Likelihood and Priors

What does it mean to constrain a nuisance parameter? How can penalty terms and priors be described as constraints? How do penalty terms priors compare? How does this fit in a Frequentist and Bayesian framework?

3.7.3. Monte Carlo Propagation and Covariance Matrix Approach

What is the Monte Carlo Propagation and the Covariance Matrix Approach. Why are they similar? Where do they differ? What is the motivation behind using them? What are the pros and cons? What is the convergence criteria for the sampling?

3.7.4. Shift Method

What is the shift method? What are its limitations and when is it needed?

4. Energy-Dependence of the Inelastic Scattering Cross Section

4.1. Introduction

A β electron's probability to scatter when travelling through the STS depends on the scattering cross section σ (2.15). The cross section σ in turn depends on the kinetic energy E_{kin} of the electron: $\sigma \equiv \sigma(E_{\text{kin}})$. This dependence has been neglected in the modeling of the electron counts in section 2.3.5. In a KATRIN measurement there exists a minimum retarding energy qU_{min} and only electrons with a kinetic energy greater than qU_{min} can reach the detector. A scattering cross section averaged over the kinetic energy of the electrons reaching the detector was assumed

$$\sigma = \sigma_{\text{avg}} = \frac{1}{\Delta E_{\text{kin}}} \int_{qU_{\text{min}}}^{qU_{\text{min}} + \Delta E_{\text{kin}}} \sigma(E_{\text{kin}}) dE_{\text{kin}} \quad \text{with} \quad \Delta E_{\text{kin}} = E_0^{\text{eff}} - qU_{\text{min}}. \quad (4.1)$$

Here, the “effective endpoint” E_0^{eff} denotes the highest kinetic energy of β electrons reaching the detector. It does not necessarily match the endpoint of the tritium β spectrum as experiment specific effects might shift it. $E_0^{\text{eff}} = 18\,575\,\text{eV}$ is assumed. Instead of an average cross section an energy dependent formula can be used. Incorporating the energy dependence makes the model more complicated and slower to compute; neglecting it may lead to wrong results. More light will be shed on both aspects within this chapter.

4.2. Cross Section Values

The total scattering cross section is a sum of the cross section for elastic and inelastic scattering.

$$\sigma(E_{\text{kin}}) = \sigma_{\text{el}} + \sigma_{\text{inel}}(E_{\text{kin}}). \quad (4.2)$$

Only the energy dependence of the inelastic scattering cross section will be considered. This is justified for now as according to [Ang+05] the cross section for elastic scattering is about an order of magnitude smaller than the one for inelastic scattering. An expression for the inelastic cross section for electrons scattering from hydrogen molecules can be found in [Liu73]. Two expressions are given, one for relativistic incident particles and one for non-relativistic incident particles. For the maximum relativistic β factor of β electrons from tritium decay one finds

$$\begin{aligned} \beta(E_{\text{kin}}, m) &= \sqrt{1 - \frac{1}{(\frac{E_{\text{kin}}}{m} + 1)^2}} \\ \beta_{\text{max}} &= \beta(E_0^{\text{eff}} \approx 18.6\,\text{keV}, m_e \approx 511\,\text{keV}) \approx 0.26 \end{aligned} \quad (4.3)$$

Traveling at approximately a forth of the speed of light, the β electrons are assumed to be non-relativistic. Then, the given expression for the energy dependent cross section is

$$\sigma(E_{\text{kin}}) = (4\pi a_0^2) \cdot \left(\frac{E_{\text{kin}}}{R}\right)^{-1} \cdot \left[C_1 \cdot \ln\left(\frac{E_{\text{kin}}}{R}\right) + C_2\right] \quad (4.4)$$

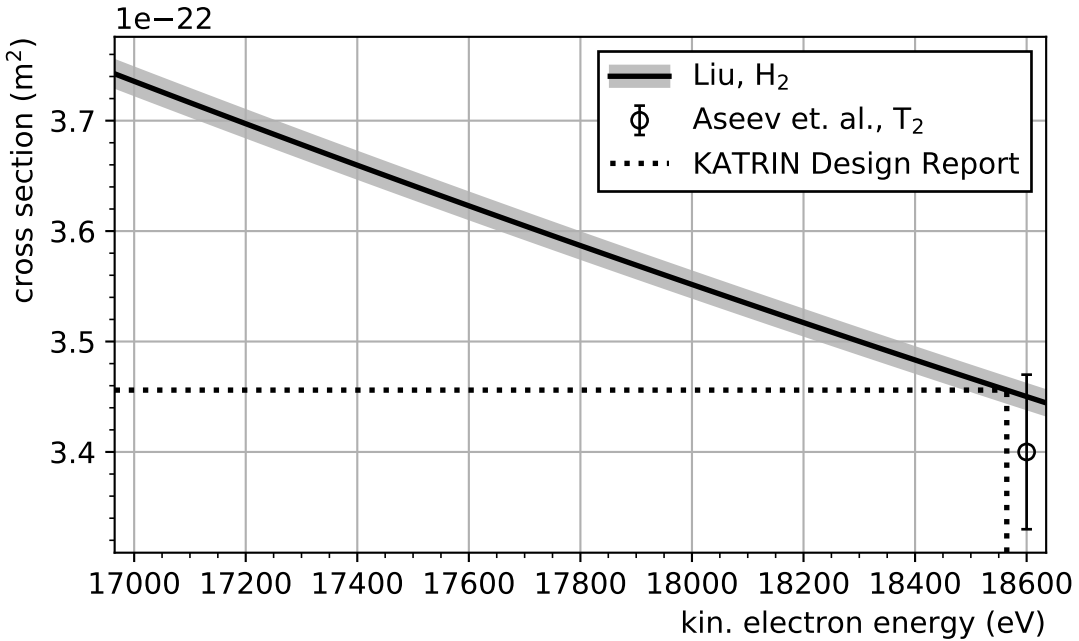


Figure 4.1.: Inelastic cross section for non-relativistic electrons scattering from molecular hydrogen isotopologues. Shown is the theoretical calculation by Liu along with its uncertainty [Liu73], the measurement by Aseev et. al. at the Troitsk experiment [AB+00] and the value stated in the KATRIN design report [Ang+05]. (The values are also listed in table 4.1.) The depicted energy interval matches the measurement interval of the First Tritium (FT) campaign.

with the Bohr radius a_0 , the Rydberg energy R and two constants given as

$$C_1 = 1.5487 \quad \text{and} \quad C_2 = 2.2212 \pm 0.0434. \quad (4.5)$$

Note that in other works $C_2 = 2.4036$ [Liu87] and $C_2 = 1.53$ [Ger75] are given. The value in (4.5) from [Liu73] was chosen to enable comparability with the KATRIN Design Report [Ang+05].

Furthermore, the total inelastic scattering cross section was measured at the Troitsk experiment and the KATRIN Design Report states a reference value. The values are listed in table 4.1. The reference value matches the theoretical calculation using (4.4) at a kinetic energy of $E_{\text{kin}} \approx 18564.4 \text{ eV}$ which would be the center of a $\Delta E_{\text{kin}} = 20 \text{ eV}$ KATRIN measurement interval. Note that in the KATRIN reference measurement interval $[E_0^{\text{eff}} - 30 \text{ eV}, E_0^{\text{eff}}]$ the cross section varies $\sim 0.14 \%$. This variation is below its theoretical uncertainty given by (4.5). In the measurement interval of the FT campaign it varies $\sim 8 \%$.

4.3. Motivation

The motivation to implement an energy dependent cross section into the SSC framework is two-fold:

Deep scans: According to [Gro15] for a neutrino mass determination with the precision goals of KATRIN, the inelastic scattering cross section has to be known with an upper uncertainty of $0.0055 \times 10^{-22} \text{ m}$ (0.16%). This requirement might be surpassed by neglecting that the scattering cross section is not constant, but varies with energy. According to table 4.1 the requirement is fulfilled in a measurement interval of $[E_0^{\text{eff}} - 30 \text{ eV}, E_0^{\text{eff}}]$. According

Table 4.1.: Energy-dependence of the inelastic scattering cross section. Listed are important values with reference to KATRIN. Except for the measured value, they are obtained using (4.4). The values are given relative to an assumed endpoint of the measured spectrum $E_0^{\text{eff}} = 18\,575 \text{ eV}$.

kin. energy	cross section (10^{-22} m)	Note
$E_0^{\text{eff}} - 1600 \text{ eV}$	3.740	largest range in FT campaign
$E_0^{\text{eff}} - 30 \text{ eV}$	3.459	KATRIN reference measurement interval [Ang+05]
$E_0^{\text{eff}} - 10 \text{ eV}$	3.456	KATRIN reference value [Ang+05]
E_0^{eff}	3.454	endpoint of tritium β spectrum
18 600 eV	3.40 ± 0.07	measured at the Troitsk experiment [AB+00]

to (4.4) it is violated if the lower bound of the measurement interval is below 18 531 eV. Scans deeper into the tritium β spectrum increase the count rates and hence, improve the statistic uncertainty on the neutrino mass. Also, for the search of sterile neutrinos deeper scans are necessary. On top of that, deeper scans have already been performed e.g. in the FT campaign and help to establish an even better understanding of the KATRIN apparatus. In these cases the energy dependence is not negligible.

Comparability: A possible cross-check for software is its comparison to other software that was developed independently. SSC is part of a data fitting suit. Other fitting software exists within the KATRIN collaboration that uses an energy dependent scattering cross section, e.g. FITRIUM [Kar+19]. Furthermore, SSC is commonly cross-checked against a Monte-Carlo particle tracking software called KASSIOPEIA [KAT19] which also implements an energy dependent scattering cross section.

4.4. Scattering Probabilities

4.4.1. Modelling

Table 4.2.: The scattering probabilities averaged over all starting positions and starting angles in the WGTS. Both the values from a Monte Carlo (MC) simulation and the values according to (2.37) are given. The later ones can also be found in [Gro15; Kle14] and in the code of the SSC framework [KAT19].

scattering count	MC particle tracking [Gro15]	equation (2.37)
0	0.415 ± 0.002	0.41334
1	0.292 ± 0.002	0.29266
2	0.166 ± 0.001	0.16733
3	0.079 ± 0.001	0.07913
4	0.031 ± 0.001	0.03178

The energy-dependence of the scattering cross section enters into the calculation of the scattering probabilities (2.20). In the derivation the dependence on the starting energy E_S was neglected. Instead an average starting energy and hence, an average scattering cross section $\sigma(18\,564.4 \text{ eV}) = 3.456 \times 10^{-22} \text{ m}^2$ was assumed. For this case table 4.2 lists the scattering probabilities averaged over all starting positions and pitch angles in the WGTS. In the energy dependent case the scattering cross section has to be adapted to the starting energy of the β electrons. In other words, the scattering probabilities follow a Poisson distribution averaged over starting positions and pitch angles of β electrons. Analogously

to the derivation in section 2.3.5 they read:

$$\mu(E_S, z_S, \theta_S) = \frac{\sigma(E_S)}{\cos \theta_S} \int_{z_S}^{L/2} \rho(z) dz \quad (4.6a)$$

$$P_l(E_S, z_S, \theta_S) = \text{Poisson}(\mu(E_S, z_S, \theta_S), l) \quad (4.6b)$$

$$\bar{P}_l(E_S) = \frac{1}{L \cdot (1 - \cos(\theta_{\max}))} \int_{-L/2}^{L/2} \int_0^{\theta_{\max}} \sin(\theta_S) \text{Poisson}(\mu(E_S, z_S, \theta_S), l) d\theta_S dz_S. \quad (4.6c)$$

Here, $\bar{P}_l(E_S)$ in the final equation (4.6c) denotes the probability of l -fold scattering for a β electron with a starting energy E_S averaged over all starting positions and pitch angles. This model will be denoted Poisson model. It is expected to be accurate for the probability of no scattering $\bar{P}_0(E_S)$.

But, depending on the required accuracy, for 1 or more scatterings this Poisson model does not necessarily hold. A scattering electron loses energy. Due to a lower energy the scattering cross section increases and the electron becomes more likely to scatter again. In other words, the probability of individual scattering processes are no longer independent. This violates one of the preconditions to model the scattering probabilities via a Poisson distribution. Another model is suggested. It assumes a constant gas density ρ , a fixed energy loss of ϵ per scattering and a source length of L :

$$\mu(E, \theta_S) = \frac{\sigma(E)\rho L}{\cos \theta_S} \quad (4.7a)$$

$$p_0(E, \theta_S, n) = \left(1 - \frac{\mu(E, \theta_S)}{N}\right)^n \quad (4.7b)$$

$$p_l(E, \theta_S, n) = \sum_{k=l}^n p_{l-1}(E, \theta_S, k-1) (1 - p_0(E - (l-1)\epsilon, \theta_S, 1)) p_0(E - l\epsilon, \theta_S, n-k) \quad (4.7c)$$

$$\bar{p}_l(E, \theta_S) = \frac{1}{L} \int_0^L p_l(E, \theta_S, \left\lceil N \frac{z_S}{L} \right\rceil) dz_S \quad (4.7d)$$

$$P_l^*(E_S, \theta_S) = \lim_{N \rightarrow \infty} \bar{p}_l(E_S, \theta_S) \quad (4.7e)$$

$$\bar{P}_l^*(E_S) = \frac{1}{1 - \cos \theta_{\max}} \int_0^{\theta_{\max}} P_l^*(E_S, \theta_S) d\theta_S. \quad (4.7f)$$

Here, $\bar{P}_l^*(E_S)$ in the final equation (4.7f) denotes the probability of l -fold scattering for a β electron with a starting energy E_S averaged over all starting positions and pitch angles assuming a fixed energy loss ϵ per scattering. This model will be denoted extended model. A descriptive derivation is given in appendix A.

The extended model is evaluated numerically as it includes one limit and two integrals. A balance between the numerical accuracy and the evaluation run time had to be found. Details can be found in the appendix A.1. The probability for 1-fold scattering could be calculated with an accuracy on the 10^{-5} level and for 2-fold scattering with an accuracy on the 10^{-3} level.

The suggested extended model is only valid for a fixed energy loss per scattering ϵ . The value $\epsilon = 14.1$ eV was chosen as it is the most probable energy loss for electrons travelling through tritium gas according to [AB+00]. A more accurate description would use the energy loss probability density. This has not yet been considered.

Figure 4.2 shows the Poisson model along with the suggested extended model. The results are discussed in the following paragraphs.

Model compatibility

For 1-fold scattering the difference between the Poisson and the extended model is on the 10^{-4} level. For 2-fold scattering the accuracy of the numerical evaluation of the extended model is not yet sufficient to distinguish it from the Poisson model. Table 4.2 lists the scattering probabilities for an energy independent Poisson model and a reference cross section $\sigma(18\,564.4\,\text{eV}) = 3.456 \times 10^{-22}\,\text{m}$ given in the KATRIN Design Report [Ang+05]. It also lists the outcome of a Monte Carlo simulation taken from [Gro15]. As expected the energy dependent Poisson model recovers the energy independent model exactly at the corresponding energy of 18 564.4 eV. Furthermore, within the endpoint region of the tritium β spectrum all models match the Monte Carlo simulation within its uncertainty.

Trend of energy-dependence

For a decreasing starting energy of β electrons the probability for no and 1-fold scattering also decreases while the probability for 2-fold scattering increases. This is expected for the following reasons. For a starting energy of $E_S = 18\,564.4\,\text{eV}$ the expected amount of scatterings μ (4.6a) averaged over all starting positions z_S and pitch angles θ_S is

$$\bar{\mu} = \frac{1}{L \cdot (1 - \cos(\theta_{\max}))} \int_{-L/2}^{L/2} \int_0^{\theta_{\max}} \sin(\theta_S) \mu(E_S, z_S, \theta_S) d\theta_S dz_S = 1.077. \quad (4.8)$$

In other words, β electrons with a starting energy near the endpoint of the tritium β spectrum are expected to scatter around $\bar{\mu} = 1.077$ times when travelling through the WGTS. If the starting energy decreases and hence, scattering becomes more likely it becomes more likely to scatter more than $\bar{\mu}$ times and less likely to scatter less than $\bar{\mu}$ times. Thus, the probability for no and 1-fold scattering decreases along with the starting energy of the β electrons. At the same time the probability for more than 1 scatterings increases for lower starting energies. This intuitive reasoning is also reflected by deriving the scattering probabilities (4.6b) for the starting energy where μ denotes the expected scattering count (4.6a)

$$\frac{dP_l(E_S, z_S, \theta_S)}{dE_S} = \underbrace{\text{Poisson}(\mu(E_S, z_S, \theta_S), l)}_{\geq 0} \cdot \underbrace{\left(\frac{l}{\mu(E_S, z_S, \theta_S)} - 1 \right)}_{(*)} \cdot \underbrace{\frac{\int_{z_S}^L \rho(z) dz}{L \cos \theta_S}}_{>0} \cdot \underbrace{\frac{d\sigma(E_S)}{dE_S}}_{<0}. \quad (4.9)$$

The sign of the derivative is determined by the sign of $(*)$ which follows approximately the above reasoning being negative for $l < \bar{\mu}$ and positive for $l > \bar{\mu}$.

4.5. Performance and Accuracy Considerations

The suggested extended model (4.7) at its current stage is computationally too expensive to be used in a fitting procedure. Note that a similar model has been derived for a fixed change of the pitch angle θ per scattering in [Gro15]. This model for angular changes is implemented in the SSC software and can be used in fitting procedures. Though, an important difference is that the determination of the count rate requires an integral over the starting energy E_S in (2.10). Hence, the energy dependent scattering probabilities have to be recomputed in every step of the numerical integration. This is not the case for the model considering the angular changes.

Albeit the energy dependent Poisson model might not fully hold in the case of an energy dependent cross section, figure 4.2 shows that for larger measurement intervals it is more accurate than assuming energy independent scattering probabilities. Hence, it is a reasonable choice to implement the energy dependent Poisson model into the SSC software. This was

done. As mentioned the energy dependent scattering probabilities have to be recomputed in every step of the numerical integration in (2.10) over the β electron energy. The impact on the run time was probed for 5 different MTDs. They differ in the amount and range of retarding potentials. Both aspects should influence the run time. The run time should be approximately linear in the amount of retarding potentials. The run time should get longer the wider the range of the retarding potentials is as the numerically evaluated integral over energies in (2.10) then stretches over a wider range. Figure 4.3 shows that the run times increase by a factor of approximately 40 – 120 between assuming a constant cross section and an energy dependent one.

4.6. Effect on Neutrino Mass Determination

ToDo

[**Numbers can not be reconciled with shifting the cross section. What to do about it?**] In order to determine the influence of the energy dependence of the scattering cross section on the neutrino mass determination the so-called “shift method” was used. A description can e.g. be found in [Sei19]. [**Write own description**] In short, an integrated rate using the energy dependent Poisson model for the scattering probabilities was simulated and fitted to a model using the constant Poisson model. One obtains a deviation of the fitted and simulated neutrino mass, the neutrino mass shift. The procedure was repeated for multiple measurement intervals using the settings from the KATRIN Design Report [Ang+05] for a 3-year measurement. A comparison of the statistical uncertainty on the neutrino mass and its shift is shown in figure 4.4 depending on the measurement interval. For a measurement interval of approximately 35 eV the shift and the statistical uncertainty are approximately equal

$$\sigma(m_\nu) \approx \sqrt{0.015\text{eV}} = 122 \text{ meV (68 \% C.L.)} . \quad (4.10)$$

Extending the Measurement Interval

In spring 2019 the so-called KNM1 campaign started. The measurement interval was 90 eV. The MTD had been optimized according to the up-to-date status of the KATRIN experiment which did not match the KATRIN Design Report in all aspects. The study on the neutrino mass shift was redone scaling the MTD of the KNM1 campaign to 3 years and using the corresponding KNM1-settings. The neutrino mass shift then would be 297 meV.

4.7. Conclusion and Outlook

The energy dependence of the scattering cross section enters into the calculation of the scattering probabilities. An accurate modelling of the energy dependent scattering probabilities is challenging due to performance reasons, but modelling them according to a Poisson distribution is possible. It was shown that the difference between the Poisson model and a more accurate model for 1-fold scattering is on the 10^{-4} level. The cases for more than 1 scatterings need further investigation. Also a fixed energy loss per scattering was assumed instead of a energy loss probability distribution. Future work might consider these aspects and what influence a more accurate modelling on the scattering probabilities has on the neutrino mass determination.

Given the KATRIN uncertainty budget, when modelling the energy dependent scattering probabilities via a Poisson distribution, the energy dependence of the scattering cross section is not negligible for measurement intervals that extend more than 35 eV below the endpoint of the tritium β spectrum.

Including the energy dependence in the analysis increases the run time of the fitting procedure significantly. Future work might consider to precalculate the scattering probabilities for different fixed energies and use interpolation techniques for energies in-between the fixed ones.

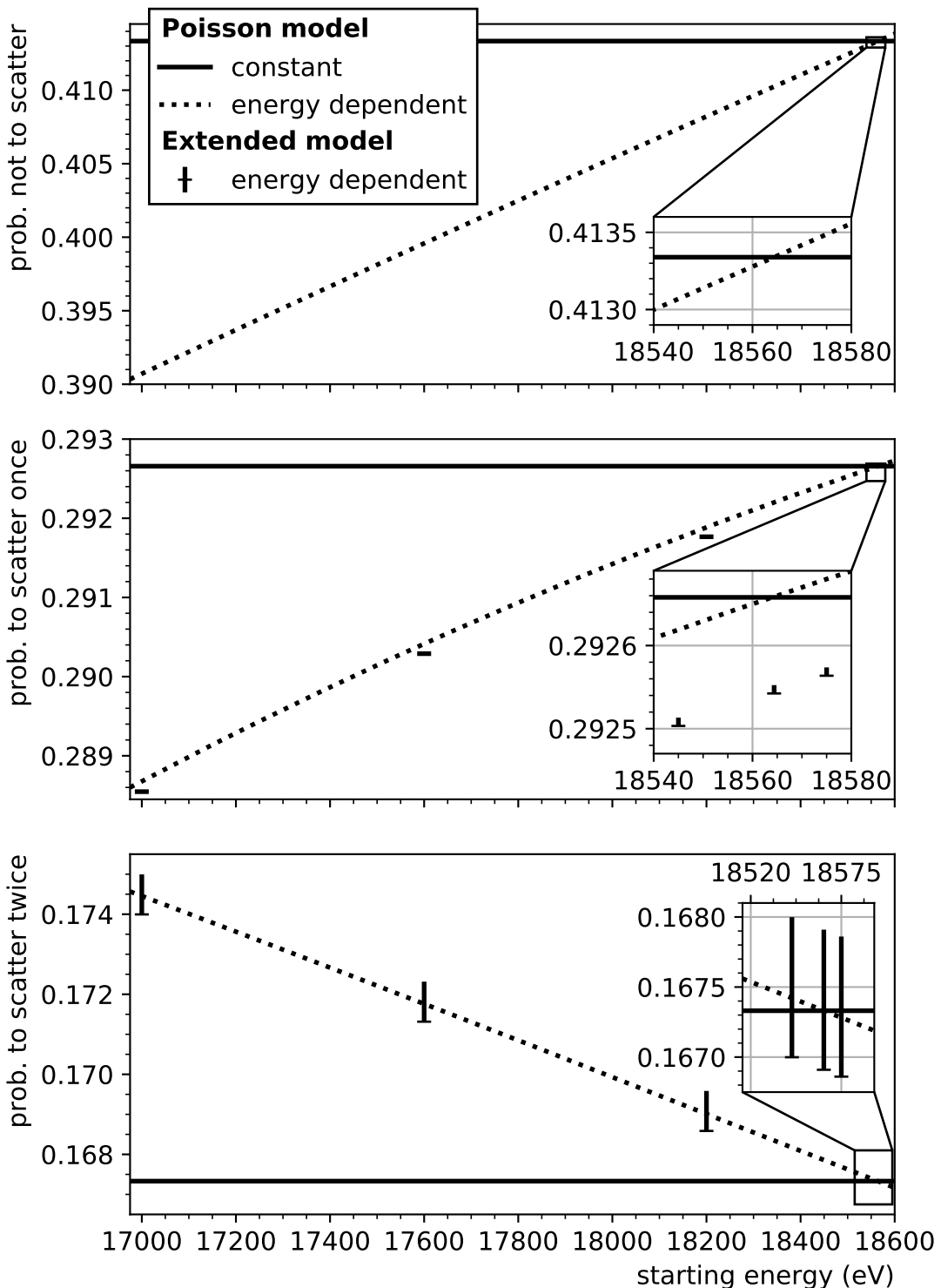


Figure 4.2.: Scattering probabilities. Shown are from top to bottom the probability for no, 1-fold and 2-fold scattering averaged over all starting positions and starting pitch angles of β electrons. Depending on the required accuracy, for 1-fold and 2-fold scattering the Poisson model does not hold. The markers show an extended model as described in the text. Its numerical evaluation suffers from a one-sided uncertainty (of $\sim 10^{-5}$ for 1-fold and $\sim 10^{-3}$ for 2-fold scattering) depicted as uncertainty bars. The inset shows an energy span around the endpoint of the tritium β spectrum. The full energy range matches the measurement interval of the First Tritium (FT) campaign.

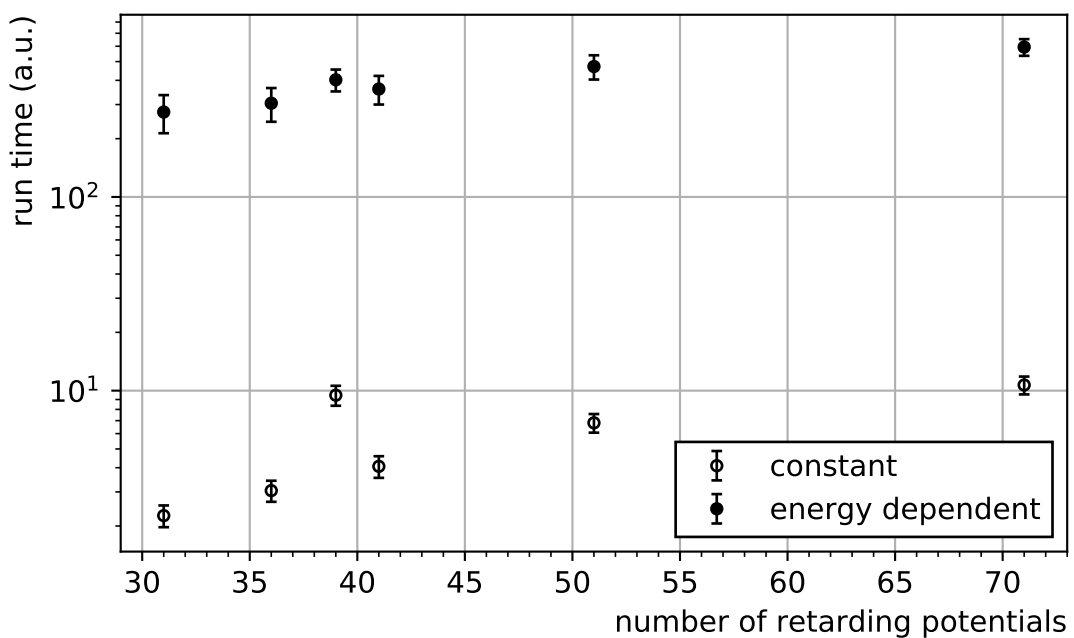


Figure 4.3.: Run times comparison between using an energy dependent and independent cross section. Shown are the run times for a fit of a simulated model to itself for different MTDs. The MTDs for the ranges 20, 25, 30, 40 and 50 eV are taken from the KATRIN design report [Ang+05] and have a rising number of retarding potentials. A further 90 eV-wide MTD of the KNM1 campaign was used. It contains 39 retarding potentials. The corresponding run time lies above the trend line as the width of the measurement interval is wider. For each MTD 30 fits were performed. The run times were clocked for a constant and an energy dependent cross section.

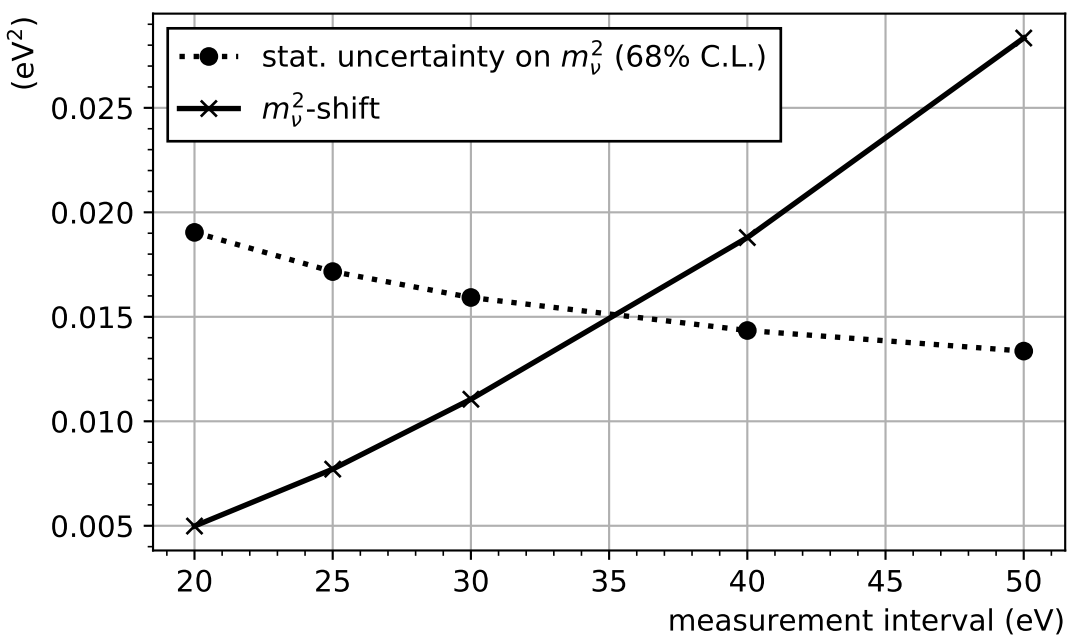


Figure 4.4.: Neutrino mass shift due to an energy dependent inelastic scattering cross section as calculated by SSC for 5 measurement intervals. The configuration for the calculation, especially the measurement time distribution (MTD), follows the KATRIN Design Report [Ang+05]. For comparison the statistical uncertainty is plotted as well. It is derived from the profile likelihood. The lines between the 5 markers are linear interpolations.

5. (Theoretical Corrections to the β Decay Spectrum)

5.1. Motivation

What are theoretical corrections?

5.2. Application to Data

What is the effect on the parameters of interest? How can it be explained?

6. (Energy Loss Normalization on First Tritium)

7. Studies using the Preliminary KATRIN Energy Loss Model

7.1. The Preliminary KATRIN Energy Loss Model

Which systematic effects were considered? What are the quantified uncertainties on them and where do these numbers come from? Why this selection?

7.2. Neutrino Mass Sensitivity

7.2.1. Motivation

Why combining systematics? What was possible in the scope of this thesis? What does this thesis try to show?

7.2.2. Methodology

What is the sensitivity on the parameters of interest? What is the z score and shrinkage for all parameters?

7.2.3. Model Configuration

Which model configuration (MTD, Slicing, Eloss-Model, FSD Binning, ...) was chosen and why?

7.2.4. Results

7.3. Application to Data

8. Conclusions

Appendix

A. Energy-Dependence of the Scattering Probabilities

A model for energy dependent scattering probabilities is derived. The expected amount of scatterings for a β electron when travelling through the whole WGTS volume of length L filled with a gas of constant density ρ is

$$\mu(E, \theta_S) = \frac{\sigma(E)\rho L}{\cos \theta_S}, \quad (\text{A.1})$$

where E denotes the electron's kinetic energy; θ_S the starting pitch angle; and $\sigma(E)$ the energy dependent scattering cross section.

The volume of the WGTS is divided into N slices of equal width $w = L/N$. N is chosen sufficiently large that the probability for a β electron to scatter twice within one slice is essentially zero. Then, for large N the probability to scatter within one slice is $\mu(E, \theta_S)/N$. The probability not to scatter within n slices is

$$p_0(E, \theta_S, n) = \left(1 - \frac{\mu(E, \theta_S)}{N}\right)^n. \quad (\text{A.2})$$

Using the well known limit for the Euler constant, one obtains for $n = N$ and $N \rightarrow \infty$ that p_0 is a Poisson distribution with expectation μ evaluated at 0

$$\lim_{N \rightarrow \infty} p_0(E, \theta_S, N) = \lim_{N \rightarrow \infty} \left(1 - \frac{\mu(E, \theta_S)}{N}\right)^N = e^{-\mu(E, \theta_S)}. \quad (\text{A.3})$$

Assuming a constant energy loss per scattering of ϵ the probability to scatter l times within n slices can be expressed recursively

$$p_l(E, \theta_S, n) = \underbrace{\sum_{k=l}^n}_{(4)} \underbrace{p_{l-1}(E, \theta_S, k-1)}_{(1)} \underbrace{(1 - p_0(E - (l-1)\epsilon, \theta_S, 1))}_{(2)} \underbrace{p_0(E - l\epsilon, \theta_S, n-k)}_{(3)}. \quad (\text{A.4})$$

The terms have the following meaning:

- (1) Probability to scatter $l-1$ times within $k-1$ slices with a kinetic energy of E .
- (2) Probability to scatter once within the k th slice with a kinetic energy of $E - (l-1)\epsilon$.
- (3) Probability not to scatter within the remaining $N-k$ slices.
- (4) Sum over all slices k . The sum starts at l because the probability to scatter $l-1$ times within less than $k = l-1$ slices (term (1)) is 0.

The probability to scatter l times can be averaged over all starting positions. The averaging sum can be further approximated by an integral as this helps cutting down on run time in a numerical evaluation

$$\bar{p}_l(E, \theta_S) = \sum_{n_S}^N p_l(E, \theta_S, n_S) \approx \frac{1}{L} \int_0^L p_l(E, \theta_S, \left\lfloor N \frac{z_S}{L} \right\rfloor) dz_S. \quad (\text{A.5})$$

Then the limit $N \rightarrow \infty$ is applied

$$P_l^*(E_S, \theta_S) = \lim_{N \rightarrow \infty} \bar{p}_l(E_S, \theta_S) \quad (\text{A.6})$$

$P_l^*(E_S, \theta_S)$ denotes the probability for a β electron to scatter l times when travelling through the whole WGTS with a starting energy E_S and pitch angle θ_S averaged over all starting positions. Finally, this expression has to be averaged over all starting pitch angles in order to obtain the energy dependent scattering probabilities

$$\bar{P}_l^*(E_S) = \frac{1}{1 - \cos \theta_{\max}} \int_0^{\theta_{\max}} P_l^*(E_S, \theta_S) d\theta_S. \quad (\text{A.7})$$

A.1. Numerical Evaluation

The energy dependent probability to scatter once \bar{P}_1^* in (A.7) was evaluated numerically. In (A.6) taking the limit $N \rightarrow \infty$ was replaced by choosing a large N . The averaging integral over the starting positions (A.5) and pitch angles (A.7) was computed using Gaussian quadrature.

Figure A.1 shows the result in dependence of N and the order of the Gaussian quadrature. Both should be chosen as low as possible to cut down on run time but sufficiently high for the required accuracy. As a cross check, for an energy loss of $\epsilon = 0$ eV per scattering, the suggested extended model (A.7) must recover the Poisson model (see (4.6)). For $N = 10^6$ and using Gaussian quadrature of order 5, they differ approximately 3×10^{-6} . Furthermore, the numerical calculation converges from below, which can be interpreted as a one-sided numerical inaccuracy. The calculations for $\epsilon = 14.1$ eV are shown in the lower row of figure A.1. They also show convergence on the 10^{-5} level. Conclusively, the results make it plausible to assume a one-sided numerical inaccuracy on the 10^{-5} level for $N = 10^5$ and using Gaussian quadrature of order 5 for the integrals.

The corresponding run time to compute \bar{P}_1^* is in $\mathcal{O}(N)$ as it requires a sum over all N slices. Note that the extended model is defined recursively and therefore, the run time for l -fold scattering is in $\mathcal{O}(N^l)$. Hence, computing the probability for 2-fold scattering would take 500000 times as long as for 1-fold scattering for the same 10^{-5} accuracy. This was found not to be feasible. For 2-fold scattering $N = 5000$ and also Gaussian quadrature of order 5 was chosen for a numerical accuracy on the 10^{-3} level.

B. First Tritium Data

What is First Tritium? Which data was selected?

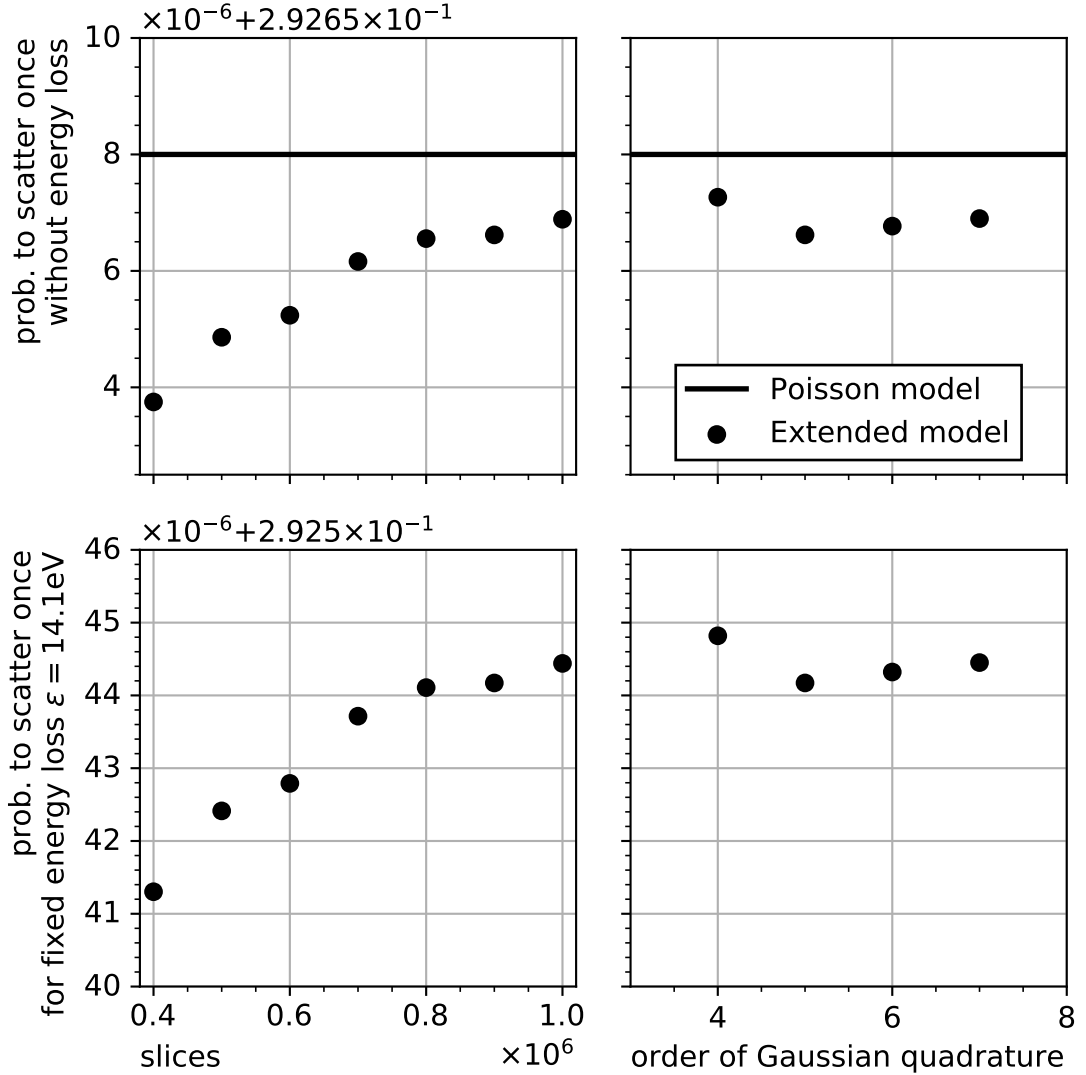


Figure A.1.: Numerical accuracy of the extended model for the scattering probabilities. The extended model is given by (A.6). The left column shows the dependence on the number of slices of the WGTS. The right column shows the order of Gaussian quadrature that was used to evaluate the two integrals in the model. For the left column the order of Gaussian quadrature was fixed to 5. For the right column the number of slices was fixed to 5×10^5 . The upper row shows the extended model for no energy loss per scattering (markers). Its exact solution is given by the Poisson model (see (4.6)). The lower row shows the model for an energy loss of 14.1 eV per scattering. The results make it plausible to assume a one-sided numerical inaccuracy on the 10^{-5} level for $N = 10^5$ and using Gaussian quadrature of order 5.

Acronyms

BIXS beta-induced X-ray spectroscopy.

CKrS condensed ^{83m}Kr source.

CPS cryogenic pumping section.

DPS differential pumping section.

EMCS earth magnetic field compensation system.

FBM forward beam monitor.

FPD focal plane detector.

FT First Tritium.

KNM1 KATRIN Neutrino Mass Measurement 1.

LARA laser Raman system.

LEP Large Electron Positron Collider.

LFCS low-field correction system.

MAC-E magnetic adiabatic collimation with electrostatic filtering.

MLE maximum likelihood estimator.

MTD measurement time distribution.

PULCINELLA precision ultra-low current integrating normalization electrometer for low-level analysis.

RMMS radial magnetic measuring system.

SDS spectrometer and detector section.

SM Standard Model of particle physics.

SSC source and spectrum calculation.

STS source and transport section.

TLK Tritium Laboratory Karlsruhe.

VMMS vertical magnetic measuring system.

WGTS windowless gaseous tritium source.

Bibliography

- [AA+13] B. Aharmim, S. N. Ahmed, et al. “Combined analysis of all three phases of solar neutrino data from the Sudbury Neutrino Observatory”. In: *Phys. Rev. C* 88 (2 Aug. 2013), p. 025501. DOI: [10.1103/PhysRevC.88.025501](https://doi.org/10.1103/PhysRevC.88.025501).
- [AB+00] V. Aseev, A. Belesev, et al. “Energy loss of 18 keV electrons in gaseous T and quench condensed D films”. In: *The European Physical Journal D - Atomic, Molecular, Optical and Plasma Physics* 10.1 (Mar. 2000), pp. 39–52. ISSN: 1434-6079. DOI: [10.1007/s100530050525](https://doi.org/10.1007/s100530050525).
- [AB+05] M. Altmann, M. Balata, et al. “Complete results for five years of GNO solar neutrino observations”. In: *Physics Letters B* 616.3 (2005), pp. 174–190. DOI: <https://doi.org/10.1016/j.physletb.2005.04.068>.
- [AB+15] J. Amsbaugh, J. Barrett, et al. “Focal-plane detector system for the KATRIN experiment”. In: *Nuclear Instruments and Methods in Physics Research Section A: Accelerators, Spectrometers, Detectors and Associated Equipment* 778 (2015), pp. 40–60. ISSN: 0168-9002. DOI: <https://doi.org/10.1016/j.nima.2014.12.116>.
- [AB+16] M. Arenz, M. Babutzka, et al. “Commissioning of the vacuum system of the KATRIN main spectrometer”. In: *Journal of Instrumentation* 11.04 (Apr. 2016), P04011–P04011. DOI: [10.1088/1748-0221/11/04/p04011](https://doi.org/10.1088/1748-0221/11/04/p04011).
- [AB+96] K. Assamagan, C. Brönnimann, et al. “Upper limit of the muon-neutrino mass and charged-pion mass from momentum analysis of a surface muon beam”. In: *Phys. Rev. D* 53 (11 June 1996), pp. 6065–6077. DOI: [10.1103/PhysRevD.53.6065](https://doi.org/10.1103/PhysRevD.53.6065).
- [AB17] D. N. Abdurashitov and A. I. o. Belesev. “Electron scattering on hydrogen and deuterium molecules at 14–25 keV by the ‘Troitsk nu-mass’ experiment”. In: *Physics of Particles and Nuclei Letters* 14.6 (Nov. 2017), pp. 892–899. ISSN: 1531-8567. DOI: [10.1134/S1547477117060024](https://doi.org/10.1134/S1547477117060024).
- [Acc+98] M. Acciarri et al. “Determination of the number of light neutrino species from single photon production at LEP”. In: *Physics Letters B* 431.1 (1998), pp. 199–208. DOI: [https://doi.org/10.1016/S0370-2693\(98\)00519-X](https://doi.org/10.1016/S0370-2693(98)00519-X).
- [AG+09] J. N. Abdurashitov, V. N. Gavrin, et al. “Measurement of the solar neutrino capture rate with gallium metal. III. Results for the 2002–2007 data-taking period”. In: *Phys. Rev. C* 80 (1 July 2009), p. 015807. DOI: [10.1103/PhysRevC.80.015807](https://doi.org/10.1103/PhysRevC.80.015807).
- [Agh+18] N. Aghanim et al. *Planck 2018 results. VI. Cosmological parameters*. 2018. arXiv: [1807.06209 \[astro-ph.CO\]](https://arxiv.org/abs/1807.06209).
- [Ago+18] M. Agostini et al. “Improved limit on neutrinoless double- β decay of ^{76}Ge from GERDA phase II”. In: *Phys. Rev. Lett.* 120.13 (2018), p. 132503. DOI: [10.1103/PhysRevLett.120.132503](https://doi.org/10.1103/PhysRevLett.120.132503). arXiv: [1803.11100 \[nucl-ex\]](https://arxiv.org/abs/1803.11100).

- [Ang+05] J. Angrik et al. “KATRIN design report 2004”. In: *Wissenschaftliche Berichte/Forschungszentrum Karlsruhe* 7090 (2005).
- [Ase+11] V. N. Aseev et al. “An upper limit on electron antineutrino mass from Troitsk experiment”. In: *Phys. Rev.* D84 (2011), p. 112003. DOI: 10.1103/PhysRevD.84.112003. arXiv: 1108.5034 [hep-ex].
- [Bab14] M. Babutzka. “Design and development for the rearsection of the KATRIN experiment”. PhD thesis. KIT, 2014. DOI: 10.5445/IR/1000045598.
- [Bar+98] R. Barate et al. “An Upper limit on the tau-neutrino mass from three-prong and five-prong tau decays”. In: *Eur. Phys. J.* C2 (1998), pp. 395–406. DOI: 10.1007/s100520050149.
- [Bau14] S. Bauer. “Energy calibration and stability monitoring of the KATRIN experiment”. PhD thesis. WWU, 2014.
- [BC38] H. A. Bethe and C. L. Critchfield. “The formation of deuterons by proton combination”. In: *Phys. Rev.* 54 (4 Aug. 1938), pp. 248–254. DOI: 10.1103/PhysRev.54.248.
- [Bec00] H. Becquerel. “Contribution à l’étude du rayonnement du radium”. In: *J. Phys. Theor. Appl.* 9.1 (1900), pp. 190–199.
- [Bec95] H. Becquerel. “Sur les radiations invisibles émises par les corps phosphorescents”. In: *Comptes rendus Acad des Sciences* 122 (1895), pp. 501–503.
- [Bet39] H. A. Bethe. “Energy production in stars”. In: *Phys. Rev.* 55 (5 Mar. 1939), pp. 434–456. DOI: 10.1103/PhysRev.55.434.
- [Boh32] N. Bohr. “Faraday lecture. Chemistry and the quantum theory of atomic constitution”. In: *J. Chem. Soc.* (0 1932), pp. 349–384. DOI: 10.1039/JR9320000349.
- [BPR15] L. I. Bodine, D. S. Parno, and R. G. H. Robertson. “Assessment of molecular effects on neutrino mass measurements from tritium β decay”. In: *Phys. Rev. C* 91 (3 Mar. 2015), p. 035505. DOI: 10.1103/PhysRevC.91.035505.
- [CD+98] B. T. Cleveland, J. Davis, et al. “Measurement of the solar electron neutrino flux with the Homestake chlorine detector”. In: *Astrophys. J.* 496 (1998), pp. 505–526. DOI: 10.1086/305343.
- [Cha14] J. Chadwick. “Intensitätsverteilung im magnetischen Spectrum der β -Strahlen von Radium B + C”. In: *Verhandl. Dtsc. Phys. Ges.* 16 (1914), p. 383.
- [CR+56] C. L. Cowan, F. Reines, et al. “Detection of the free neutrino: a confirmation”. In: *Science* 124.3212 (1956), pp. 103–104. ISSN: 0036-8075. DOI: 10.1126/science.124.3212.103.
- [DG+62] G. Danby, J. M. Gaillard, et al. “Observation of high-energy neutrino reactions and the existence of two kinds of neutrinos”. In: *Phys. Rev. Lett.* 9 (1962), pp. 36–44. DOI: 10.1103/PhysRevLett.9.36.
- [DT+04] A. Doroshkevich, D. L. Tucker, et al. “Large scale structure in the SDSS galaxy survey”. In: *Astron. Astrophys.* 418 (2004), pp. 7–23.
- [EB+14] M. Erhard, S. Bauer, et al. “High-voltage monitoring with a solenoid retarding spectrometer at the KATRIN experiment”. In: *Journal of Instrumentation* 9.06 (June 2014), P06022–P06022. DOI: 10.1088/1748-0221/9/06/p06022.
- [EB+18] M. Erhard, J. Behrens, et al. “Technical design and commissioning of the KATRIN large-volume air coil system”. In: *Journal of Instrumentation* 13.02 (Feb. 2018), P02003–P02003. DOI: 10.1088/1748-0221/13/02/p02003.

- [EG+19] I. Esteban, Gonzalez-Garcia, M. C., et al. “Global analysis of three-flavour neutrino oscillations: synergies and tensions in the determination of θ_{23} , δ_{CP} , and the mass ordering”. In: *Journal of High Energy Physics* 2019.1 (Jan. 2019), p. 106. ISSN: 1029-8479. DOI: 10.1007/JHEP01(2019)106.
- [EH+17] E. Ellinger, N. Haußmann, et al. “Monitoring the KATRIN source properties within the beamline”. In: *Journal of Physics: Conference Series* 888 (Sept. 2017), p. 012229. DOI: 10.1088/1742-6596/888/1/012229.
- [EW72] C. D. Ellis and W. A. Wooster. “The average energy of disintegration of radium E”. In: *Proc. R. Soc. Lond., A* 117 (1972), p. 109. DOI: 10.1098/rspa.1927.0168.
- [FC98] G. J. Feldman and R. D. Cousins. “Unified approach to the classical statistical analysis of small signals”. In: 57.7 (Apr. 1998), pp. 3873–3889. DOI: 10.1103/PhysRevD.57.3873. arXiv: physics/9711021 [physics.data-an].
- [Fer34] E. Fermi. “Versuch einer Theorie der β -Strahlen”. In: *Zeitschrift für Physik* 88.3 (1934), pp. 161–177. DOI: 10.1007/BF01351864.
- [GB+08] S. Grohmann, J. Bonn, et al. “Cryogenic design of the KATRIN source cryostat”. In: *AIP Conference Proceedings* 985.1 (2008), pp. 1277–1284. DOI: 10.1063/1.2908483.
- [Ger75] D. E. Gerhart. “Comprehensive optical and collision data for radiation action. I. H₂”. In: *The Journal of Chemical Physics* 62.3 (1975), pp. 821–832. DOI: 10.1063/1.430533.
- [GG+16] A. Gando, Y. Gando, et al. “Search for Majorana neutrinos near the inverted mass hierarchy region with KamLAND-Zen”. In: *Phys. Rev. Lett.* 117 (8 Aug. 2016), p. 082503. DOI: 10.1103/PhysRevLett.117.082503.
- [GG+58] M. Goldhaber, L. Grodzins, et al. “Helicity of neutrinos”. In: *Phys. Rev.* 109 (3 Feb. 1958), pp. 1015–1017. DOI: 10.1103/PhysRev.109.1015.
- [Gro15] S. Groh. “Modeling of the response function and measurement of transmission properties of the KATRIN experiment”. PhD thesis. KIT, 2015. DOI: 10.5445/IR/1000046546.
- [Har15] F. T. Harms. “Characterization and minimization of background processes in the KATRIN main spectrometer”. 51.03.01; LK 01. PhD thesis. KIT, 2015. DOI: 10.5445/IR/1000050027.
- [Jan15] A. Jansen. “The cryogenic pumping section of the KATRIN experiment - design studies and experiments for the commissioning”. PhD thesis. KIT, 2015. DOI: 10.5445/IR/1000047146.
- [Kar+19] C. Karl et al. *FITRIUM*. <https://nuserv.uni-muenster.de:8443/karlch/Fitrium>. 2019.
- [KAT19] KATRIN collaboration. *KATRIN analysis and simulations package (KASPER)*. <https://nuserv.uni-muenster.de:8443/katrin-git/kasper>. 2019.
- [KB+05] C. Kraus, B. Bornschein, et al. “Final results from phase II of the Mainz neutrino mass search in tritium decay”. In: *European Physical Journal C* 40 (Apr. 2005), pp. 447–468.
- [KB+19] M. Kleesiek, J. Behrens, et al. “ β -decay spectrum, response function and statistical model for neutrino mass measurements with the KATRIN experiment”. In: *The European Physical Journal C* 79.3 (Mar. 2019), p. 204. ISSN: 1434-6052. DOI: 10.1140/epjc/s10052-019-6686-7.

- [KH+18] L. Kuckert, F. Heizmann, et al. “Modelling of gas dynamical properties of the KATRIN tritium source and implications for the neutrino mass measurement”. In: *Vacuum* 158 (2018), pp. 195–205. ISSN: 0042-207X. DOI: <https://doi.org/10.1016/j.vacuum.2018.09.036>.
- [Kir98] T. Kirsten. “GALLEX solar neutrino results”. In: *Progress in Particle and Nuclear Physics* 40 (1998). Neutrinos in Astro, Particle and Nuclear Physics, pp. 85–99. ISSN: 0146-6410. DOI: [https://doi.org/10.1016/S0146-6410\(98\)00013-1](https://doi.org/10.1016/S0146-6410(98)00013-1).
- [Kle14] M. Kleesiek. “A data-analysis and sensitivity-optimization framework for the KATRIN experiment”. PhD thesis. KIT, 2014. DOI: 10.5445/IR/1000043301.
- [Kod+01] K. Kodama et al. “Observation of tau neutrino interactions”. In: *Phys. Lett.* B504 (2001), pp. 218–224. DOI: 10.1016/S0370-2693(01)00307-0.
- [Kos12] A. Kosmider. “Tritium retention techniques in the KATRIN transport section and commissioning of its DPS2-F cryostat”. PhD thesis. KIT, 2012. DOI: 10.5445/IR/1000028959.
- [LH+18] J. Letnev, W. Hazenbiller, et al. “Technical design and commissioning of a sensor net for fine-meshed measuring of the magnetic field at the KATRIN spectrometer”. In: *Journal of Instrumentation* 13.08 (Aug. 2018), T08010–T08010. DOI: 10.1088/1748-0221/13/08/t08010.
- [Liu73] J. W. Liu. “Total inelastic cross section for collisions of H₂ with fast charged particles”. In: *Phys. Rev. A* 7 (1 Jan. 1973), pp. 103–109. DOI: 10.1103/PhysRevA.7.103.
- [Liu87] J. W. Liu. “Total cross sections for high-energy electron scattering by H₂ (¹Σ_g⁺), N₂ (¹Σ_g⁺), and O₂ (³Σ_g⁻)”. In: *Phys. Rev. A* 35 (2 Jan. 1987), pp. 591–597. DOI: 10.1103/PhysRevA.35.591.
- [LL02] T. J. Loredo and D. Q. Lamb. “Bayesian analysis of neutrinos observed from supernova SN 1987A”. In: *Phys. Rev. D* 65 (6 Feb. 2002), p. 063002. DOI: 10.1103/PhysRevD.65.063002.
- [LY56] T. D. Lee and C. N. Yang. “Question of parity conservation in weak interactions”. In: *Phys. Rev.* 104 (1 1956), pp. 254–258. DOI: 10.1103/PhysRev.104.254.
- [MS86] S. P. Mikheev and A. Y. Smirnov. “Resonant amplification of neutrino oscillations in matter and solar neutrino spectroscopy”. In: *Nuovo Cim.* C9 (1986), pp. 17–26. DOI: 10.1007/BF02508049.
- [Ney37] J. Neyman. “Outline of a theory of statistical estimation based on the classical theory of probability”. In: *Philosophical Transactions of the Royal Society of London. Series A, Mathematical and Physical Sciences* 236.767 (1937), pp. 333–380. ISSN: 00804614.
- [OW08] E. W. Otten and C. Weinheimer. “Neutrino mass limit from tritium beta decay”. In: *Rept. Prog. Phys.* 71 (2008), p. 086201. DOI: 10.1088/0034-4885/71/8/086201. arXiv: 0909.2104 [hep-ex].
- [PR+12] M. Prall, P. Renschler, et al. “The KATRIN pre-spectrometer at reduced filter energy”. In: *New Journal of Physics* 14.7 (July 2012), p. 073054. DOI: 10.1088/1367-2630/14/7/073054.
- [PW+08] W. Pauli, V. Weisskopff, et al. *Wissenschaftlicher Briefwechsel mit Bohr, Einstein, Heisenberg u.a. Band II: 1930–1939*. Springer Berlin Heidelberg, 2008. ISBN: 9783540788010.

- [Rut99] E. Rutherford. “VIII. Uranium radiation and the electrical conduction produced by it”. In: *The London, Edinburgh, and Dublin Philosophical Magazine and Journal of Science* 47.284 (1899), pp. 109–163. DOI: 10.1080/14786449908621245.
- [Sei19] H. Seitz-Moskaliuk. “Characterisation of the KATRIN tritium source and evaluation of systematic effects”. PhD thesis. KIT, 2019.
- [Tan+18] M. Tanabashi et al. “Review of particle physics”. In: *Phys. Rev. D* 98 (3 Aug. 2018), p. 030001. DOI: 10.1103/PhysRevD.98.030001.
- [Tho97] J. J. Thomson. “XL. Cathode rays”. In: *The London, Edinburgh, and Dublin Philosophical Magazine and Journal of Science* 44.269 (1897), pp. 293–316. DOI: 10.1080/14786449708621070.
- [TM+09] T. Thümmler, R. Marx, et al. “Precision high voltage divider for the KATRIN experiment”. In: *New Journal of Physics* 11.10 (Oct. 2009), p. 103007. DOI: 10.1088/1367-2630/11/10/103007.
- [Tro19] N. R.-M. Trost. “Modeling and measurement of Rydberg-state mediated background at the KATRIN main spectrometer”. 51.03.01; LK 01. PhD thesis. KIT, 2019. 178 pp. DOI: 10.5445/IR/1000090450.
- [UR+09] M. Ubieto-Díaz, D. Rodríguez, et al. “A broad-band FT-ICR penning trap system for KATRIN”. In: *International Journal of Mass Spectrometry* 288.1 (2009), pp. 1–5. ISSN: 1387-3806. DOI: <https://doi.org/10.1016/j.ijms.2009.07.003>.
- [Val09] K. Valerius. “Spectrometer-related background processes and their suppression in the KATRIN experiment”. PhD thesis. WWU, 2009.
- [WA+57] C. S. Wu, E. Ambler, et al. “Experimental test of parity conservation in beta decay”. In: *Phys. Rev.* 105 (4 Feb. 1957), pp. 1413–1415. DOI: 10.1103/PhysRev.105.1413.
- [Wei38] C. F. Weizäcker. “Über Elementumwandlungen im Innern der Sterne”. In: *Phys. Zeit.* 39 (633 1938), p. 46.
- [Wol78] L. Wolfenstein. “Neutrino oscillations in matter”. In: *Phys. Rev. D* 17 (1978). [,294(1977)], pp. 2369–2374. DOI: 10.1103/PhysRevD.17.2369.
- [YP+17] C. Yèche, Palanque-Delabrouille, Nathalie, et al. “Constraints on neutrino masses from Lyman-alpha forest power spectrum with BOSS and XQ-100”. In: *JCAP* 1706.06 (2017), p. 047. DOI: 10.1088/1475-7516/2017/06/047. arXiv: 1702.03314 [astro-ph.CO].
- [Zub11] K. Zuber. *Neutrino Physics, Second Edition*. Series in High Energy Physics, Cosmology and Gravitation. Taylor & Francis, 2011. ISBN: 9781420064711.